Valley Jahn-Teller Effect in Twisted Bilayer Graphene

M. Angeli⊙,[1] E. Tosatti,[1,2,3] and M. Fabrizio[1]

[1]*International School for Advanced Studies (SISSA), Via Bonomea 265, I-34136 Trieste, Italy*
[2]*CNR-IOM Democritos, Istituto Officina dei Material,*
Consiglio Nazionale delle Ricerche, I-34136 Trieste, Italy
[3]*International Centre for Theoretical Physics (ICTP), Strada Costiera 11, I-34151 Trieste, Italy*

The surprising insulating and superconducting states of narrow-band graphene twisted bilayers have been mostly discussed so far in terms of strong electron correlation, with little or no attention to phonons and electron-phonon effects. We found that, among the 33 492 phonons of a fully relaxed $\theta = 1.08°$ twisted bilayer, there are few special, hard, and nearly dispersionless modes that resemble global vibrations of the moiré supercell, as if it were a single, ultralarge molecule. One of them, doubly degenerate at $\mathbf{\Gamma}$ with symmetry $A_1 + B_1$, couples very strongly with the valley degrees of freedom, also doubly degenerate, realizing a so-called $E \otimes e$ Jahn-Teller (JT) coupling. The JT coupling lifts very efficiently all degeneracies which arise from the valley symmetry, and may lead, for an average atomic displacement as small as 0.5 m Å, to an insulating state at charge neutrality. This insulator possesses a nontrivial topology testified by the odd winding of the Wilson loop. In addition, freezing the same phonon at a zone boundary point brings about insulating states at most integer occupancies of the four ultraflat electronic bands. Following that line, we further study the properties of the superconducting state that might be stabilized by these modes. Since the JT coupling modulates the hopping between AB and BA stacked regions, pairing occurs in the spin-singlet Cooper channel at the inter-(AB-BA) scale, which may condense a superconducting order parameter in the extended s-wave and/or $d \pm id$-wave symmetry.

　　　　　　　　　Subject Areas: Condensed Matter Physics

I. INTRODUCTION

The recent discovery of superconductivity in magic angle ($\theta \approx 1.1°$) twisted bilayer graphene (TBLG) [1–4] has stimulated intense theoretical and experimental research activity. This unexpected phenomenon occurs upon slightly doping insulating states found at fractional fillings, the latter contradicting the metallic behavior predicted by band structure calculations. Despite the huge size of the unit cell, containing more than $\approx 11\,000$ atoms, the band structure of TBLG at the first magic angle has been computed with a variety of methods, including tight binding [5–10], continuum models [11,12], and density functional theory (DFT) [13,14]. These approaches predict that all the exotic properties mentioned above arise from four extremely flat bands (FBs), located around the charge neutrality point, with a bandwidth of the order of ≈ 10–20 meV. Owing to the flatness of these bands, the fractional filling insulators found in Refs. [1,2] are

conjectured to be Mott insulators, even though rather anomalous ones, since they turn frankly metallic above a critical temperature or above a threshold Zeeman splitting in a magnetic field, features not expected from a Mott insulator. Actually, the linear size of the unit cell at the magic angle is as large as ≈ 14 nm, and the effective *on-site* Coulomb repulsion, the so-called Hubbard U, must be given by the charging energy in this large supercell projected onto the FBs, including screening effects due to the gates and to the other bands. Even neglecting the latter, the estimated $U \sim 9$ meV is comparable to the bandwidth of the FBs [15]. Since the FBs are reproducibly found in experiments [1–4,16–20] to be separated from the other bands by a gap of around ~ 30–50 meV, the actual value of U should be significantly smaller, implying that TBLG might not be more correlated than a single graphene sheet [21]. In turn, this suggests that the insulating behavior at $\nu = \pm 2$ occupancy might instead be the result of a weak-coupling Stoner or charge density wave band instability driven by electron-electron and/or electron-phonon interactions, rather than a Mott localization phenomenon.

As pointed out in Ref. [22], in order to open an insulating gap the band instability must break the twofold degeneracy at the $\mathbf{K}$ points imposed by the D_6 space group symmetry of the moiré superlattice, as well as the additional twofold

degeneracy due to the so-called valley charge conservation. This conserved quantity is associated with an emergent dynamical U(1) symmetry that appears at small twist angles, a symmetry which, unlike spatial symmetries, is rather subtle and elusive. It is therefore essential to identify a microscopic mechanism that could efficiently break this emergent symmetry, hereafter referred to as $U_v(1)$. The most natural candidate is the Coulomb repulsion [22–24], whose Fourier transform decays more slowly than that of electron hopping, possibly introducing a non-negligible coupling among the two valleys even at small twist angles. Indeed DFT-based calculations show a tiny valley splitting [13,14], almost at the limits of accuracy of the method, which is nevertheless too small to explain the insulating states found in the FBs.

Here we uncover another $U_v(1)$-breaking mechanism involving instead the lattice degrees of freedom (d.o.f.), mostly ignored so far. It must be recalled that *ab initio* DFT-based calculations fail to predict well-defined FBs separated from other bands unless atomic positions are allowed to relax [10,14,25–28], especially out of plane. That alone already demonstrated that the effects of atomic motions in the lattice are not at all negligible in TBLG, further supported by the significant phonon contribution to transport [18,29,30]. We calculate the phonon spectrum of the fully relaxed bilayer at 1.08° twist angle, which shows the presence, among the about 30 000 phonons, of a small set of very special optical modes, with C-C stretching character, very narrow and uniquely coherent over the moiré supercell Brillouin zone. Among them, we find a doubly degenerate optical mode that couples to the $U_v(1)$ symmetry much more efficiently than Coulomb repulsion seems to do in DFT calculations. A subsequent frozen-phonon tight-binding calculation shows that this mode is able to fully lift the valley degeneracy even when its lattice deformation amplitude is extremely small. Remarkably, both electrons and phonons are twofold $U_v(1)$ degenerate, and the coupling of this mode with the electron bands actually realizes an $E \otimes e$ Jahn-Teller (JT) effect [31]. This effect is able to stabilize insulating states at integer occupancies of the FBs, both even and odd. Moreover, a surprising and important additional result will be that the electron-phonon coupling magnitude controlling this process is extremely large, and not small as one could generally expect for a very narrow band. We conclude by studying the superconducting state that might be mediated by the Jahn-Teller coupling in a minimal tight-binding model of the FBs that reproduces symmetries and topological properties of the realistic band structure calculations.

This work is organized as follows. In Sec. II, we specify the geometry of the TBLG studied and define useful quantities that are used throughout the article. In Sec. III, we briefly discuss the band structure obtained by a realistic tight-binding calculation of the TBLG with fully relaxed atomic positions. The phonon spectrum and

its properties, especially focusing on special optical modes strongly coupled with the valley $U_v(1)$ symmetry, are thoroughly discussed in Sec. IV. Section VII addresses the properties of the superconducting state that might be stabilized by the particular phonon mode identified in the previous section, through a mean-field calculation using a model tight-binding Hamiltonian of the FBs. Finally, Sec. VIII is devoted to concluding remarks.

II. MOIRÉ SUPERLATTICE AND SYMMETRIES

In Fig. 1 we show the geometry of the TBLG that we use hereafter. We start from an *AA* stacked bilayer and rotate in opposite directions the two layers around the center of a hexagon by an angle 1.08°/2, leading to a unit cell with 11 164 carbon atoms. The moiré superlattice, top left-hand panel, with the reference frame defined in the top right-hand panel, possesses a full D_6 spatial symmetry. Specifically, resolving the action of each symmetry operation in the indices that identify the two layers, 1 and 2, the
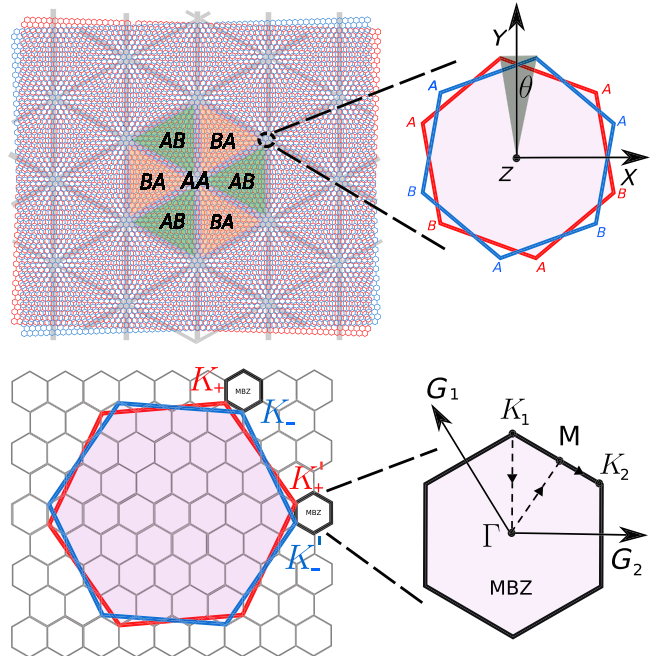

FIG. 1. Top: Moiré superlattice formed by two unrelaxed graphene layers (in blue and red) twisted by an angle θ. We indicate the different stacking regions: *AA* and the two different Bernal regions *AB* and *BA*. The domain walls (DWs) separate *AB* from *BA* regions and connect different *AA* regions. On the right, an enlargement of the *AA* stacked region is shown: two overlapping hexagons in distinct graphene layers are rotated in opposite directions around the perpendicular z axis by an angle $\theta/2$. Bottom: The folding procedure in TBLG. The original single-layer Brillouin zones (in red and blue) are folded into the mini Brillouin zone (MBZ). Two inequivalent **K** points in different layers ($\mathbf{K}_-$ and $\mathbf{K}'_+$ or $\mathbf{K}'_-$ and $\mathbf{K}_+$) are folded into the same points, $\mathbf{K}_1$ or $\mathbf{K}_2$, of the MBZ. The path $\mathbf{K}_1 \rightarrow \mathbf{\Gamma} \rightarrow \mathbf{M} \rightarrow \mathbf{K}_2$ is also shown.

TABLE I.   Nontrivial irreducible representations of the space group D_6. Each representation has the degeneracy shown in parentheses. We also list the action of the symmetry operations for each representation, where $\phi = 2\pi/3$.

	C_{3z}	C_{2x}	C_{2y}
$A_1(1)$	$+1$	$+1$	$+1$
$A_2(1)$	$+1$	-1	-1
$B_1(1)$	$+1$	$+1$	-1
$B_2(1)$	$+1$	-1	$+1$
$E_1(2)$	$\begin{pmatrix} \cos\phi & -\sin\phi \\ \sin\phi & \cos\phi \end{pmatrix}$	$\begin{pmatrix} +1 & 0 \\ 0 & -1 \end{pmatrix}$	$\begin{pmatrix} -1 & 0 \\ 0 & +1 \end{pmatrix}$
$E_2(2)$	$\begin{pmatrix} \cos\phi & -\sin\phi \\ \sin\phi & \cos\phi \end{pmatrix}$	$\begin{pmatrix} 1 & 0 \\ 0 & -1 \end{pmatrix}$	$\begin{pmatrix} 1 & 0 \\ 0 & -1 \end{pmatrix}$

two sublattices within each layer, A and B, and, finally, the two sublattices AB and BA of the moiré superlattice (see top panel of Fig. 1), we have that

(i)   the rotation C_{3z} by 120° around the z axis is diagonal in all indices, 1 and 2, A and B, and AB and BA,

(ii)   the C_{2x} rotation by 180° around the x axis interchanges 1 with 2 and A with B, but is diagonal in AB and BA,

(iii)   the C_{2y} rotation by 180° around the y axis interchanges 1 with 2 and AB with BA, but is diagonal in A and B,

(iv)   finally, the action of a C_{2z} rotation by 180° around the z axis is a composite symmetry operation obtained by noting that $C_{2z} = C_{2x} \times C_{2y}$.

In Table I we list the irreducible representations (irreps) of the D_6 space group and the action on each of them of the symmetry transformations C_{3z}, C_{2x}, and C_{2y}.

A. $U_v(1)$ valley symmetry

The mini Brillouin zone (MBZ) that corresponds to the real space geometry of Fig. 1 and its relationship with the original graphene Brillouin zones are shown in the bottom panels of Fig. 1 (for better readability, at a larger angle than the actual 1.08° which we use). Because of the chosen geometry, the Dirac point $\mathbf{K}_+$ ($\mathbf{K}'_+$) of the top layer and $\mathbf{K}'_-$ ($\mathbf{K}_-$) of the bottom one fold onto the same point, $\mathbf{K}_1$ or $\mathbf{K}_2$, of the MBZ, so that a finite matrix element of the Hamiltonian between them is allowed by symmetry. Nevertheless, as pointed out by Ref. [11], the matrix element of the one-body component of the Hamiltonian is negligibly small at small twist angles, so that the two Dirac points, hereafter named *valleys*, remain effectively independent of each other. This implies that the operator,

$$\Delta N_v = N_1 - N_2, \qquad (1)$$

where N_1 and N_2 are the occupation numbers of each valley, must commute with the noninteracting Hamiltonian of the TBLG at small angles. That operator is in fact

the generator of the $U_v(1)$ symmetry. As we see in the following (see Sec. III A), the interplay between the valley symmetry and C_{2y} is responsible for the additional twofold degeneracies beyond those of Table I in both electron band structure and phonon spectra along all the points in the MBZ invariant under that symmetry.

B. Wannier orbitals

We assume in the following Wannier orbitals (WOs) that are centered at the Wyckoff positions $2c$ of the moiré triangular superlattice, i.e., at the AB and BA region centers, even though their probability distribution has a very substantial component in other regions such as AA. The large size of the unit cell has so far originated an intense effort to find a minimal model faithfully describing the FBs' physics. While a variety of WOs centered at different Wyckoff positions has been proposed [13,22,27,32–37], our simple assumption is well suited for our purposes. The site symmetry at the Wyckoff positions $2c$ is D_3, and includes only C_{3z} and C_{2x} with irreps A_1, A_2, and E. Inspired by the symmetries of the Bloch states at the high-symmetry points [10], see Sec. III, we consider two A_1 and A_2 one-dimensional irreps (1D irreps), both invariant under C_{3z} and eigenstates of C_{2x} with opposite eigenvalues $c_{2x} = \pm 1$. In addition, we consider one two-dimensional irrep (2D irrep) E, which transforms under C_{3z} and C_{2x} as the 2D irreps in Table I, hence comprises eigenstates of C_{2x}, with opposite eigenvalues $c_{2x} = \pm 1$, which are not invariant under C_{3z}. We define on sublattice $\alpha = AB$, BA the spin-σ WO annihilation operators $\Psi_{\alpha,\mathbf{R}\sigma}$ and $\Phi_{\alpha,\mathbf{R}\sigma}$ corresponding to the two 1D irreps (Ψ) or the single 2D irrep (Φ), respectively,

$$\Psi_{\alpha,\mathbf{R}\sigma} = \begin{pmatrix} \Psi_{\alpha,1,s,\mathbf{R}\sigma} \\ \Psi_{\alpha,2,s,\mathbf{R}\sigma} \\ \Psi_{\alpha,1,p,\mathbf{R}\sigma} \\ \Psi_{\alpha,2,p,\mathbf{R}\sigma} \end{pmatrix}, \quad \Phi_{\alpha,\mathbf{R}\sigma} = \begin{pmatrix} \Phi_{\alpha,1,s,\mathbf{R}\sigma} \\ \Phi_{\alpha,2,s,\mathbf{R}\sigma} \\ \Phi_{\alpha,1,p,\mathbf{R}\sigma} \\ \Phi_{\alpha,2,p,\mathbf{R}\sigma} \end{pmatrix}, \qquad (2)$$

where the subscript s refers to $c_{2x} = +1$ and p refers to $c_{2x} = -1$, while the labels 1 and 2 refer to the two valleys. It is implicit that each component is itself a spinor that includes fermionic operators corresponding to different WOs that transform like the same irrep. We shall combine the operators of different sublattices into a single spinor:

$$\Psi_{\mathbf{R}\sigma} = \begin{pmatrix} \Psi_{AB,\mathbf{R}\sigma} \\ \Psi_{BA,\mathbf{R}\sigma} \end{pmatrix}, \qquad \Phi_{\mathbf{R}\sigma} = \begin{pmatrix} \Phi_{AB,\mathbf{R}\sigma} \\ \Phi_{BA,\mathbf{R}\sigma} \end{pmatrix}. \qquad (3)$$

We further introduce three different Pauli matrices σ_a that act in the moiré sublattice space (AB, BA), μ_a in the $c_{2x} = \pm 1$ space (s, p), and τ_a in the valley space (1, 2), where $a = 0, 1, 2, 3$, $a = 0$ denoting the identity.

With these definitions, the generator (1) of the valley $U_v(1)$ symmetry becomes simply

$$\Delta N_v = \sum_{\mathbf{R}\sigma} (\Psi_{\mathbf{R}\sigma}^\dagger \sigma_0 \tau_3 \mu_0 \Psi_{\mathbf{R}\sigma} + \Phi_{\mathbf{R}\sigma}^\dagger \sigma_0 \tau_3 \mu_0 \Phi_{\mathbf{R}\sigma}). \quad (4)$$

It is now worth deriving the expression of the space group symmetry operations in this notation and representation. By definition, the C_{2x} transformation corresponds to the simple operator

$$\mathcal{C}_{2x}(\Psi_{\mathbf{R}\sigma}) = \sigma_0 \tau_0 \mu_3 \Psi_{C_{2x}(\mathbf{R})\sigma},$$
$$\mathcal{C}_{2x}(\Phi_{\mathbf{R}\sigma}) = \sigma_0 \tau_0 \mu_3 \Phi_{C_{2x}(\mathbf{R})\sigma}. \quad (5)$$

The 180° rotation around the z axis that connects sublattice AB with BA of each layer (C_{2z}) is not diagonal in the valley indices and can be represented by [13,33]

$$\mathcal{C}_{2z}(\Psi_{\mathbf{R}\sigma}) = \sigma_1 \tau_1 \mu_0 \Psi_{C_{2z}(\mathbf{R})\sigma},$$
$$\mathcal{C}_{2z}(\Phi_{\mathbf{R}\sigma}) = \sigma_1 \tau_1 \mu_0 \Phi_{C_{2z}(\mathbf{R})\sigma}. \quad (6)$$

Finally, since $C_{2y} = C_{2z} \times C_{2x}$, then

$$\mathcal{C}_{2y}(\Psi_{\mathbf{R}\sigma}) = \sigma_1 \tau_1 \mu_3 \Psi_{C_{2y}(\mathbf{R})\sigma},$$
$$\mathcal{C}_{2y}(\Phi_{\mathbf{R}\sigma}) = \sigma_1 \tau_1 \mu_3 \Phi_{C_{2y}(\mathbf{R})\sigma}. \quad (7)$$

III. LATTICE RELAXATION AND SYMMETRY ANALYSIS OF THE BAND STRUCTURE

Since the TBLG must undergo, relative to the ideal superposition of two rigid graphene layers, a substantial lattice relaxation, whose effects have also been observed in recent experiments [16,17,38,39], we performed lattice relaxations via classical molecular dynamics techniques using state-of-the-art force fields, allowing for both in-plane and out-of-plane deformations. The details about the relaxation procedure are in the Appendix A and are essentially those in Ref. [10]. It is well known [10,14,25, 28,40–44] that, after full relaxation, the energetically less favorable AA regions shrink while the Bernal-stacked ones, AB and BA, expand in the (x,y) plane. In addition, the interlayer distance along z of the AA regions increases with respect to that of the AB and BA zones, leading to significant out-of-plane buckling deformations, genuine "corrugations" of the graphene layers, which form protruding AA bubbles. The main effect of the layer corrugations is to enhance the band gaps between the FBs and those above and below [10,14,45], important even if partially hindered by the hexagonal-boron-nitride- (h-BN) encapsulation of the samples during the experiments [1]. Moreover, since both the AB and BA triangular domains have expanded, the initially broad crossover region between them sharpens into narrow domain walls (DWs) that merge at the AA centers in the moiré superlattice (see Fig. 1). The electronic structure shown in Fig. 2 is obtained with standard tight-binding calculations, see Appendix A for further details, with the
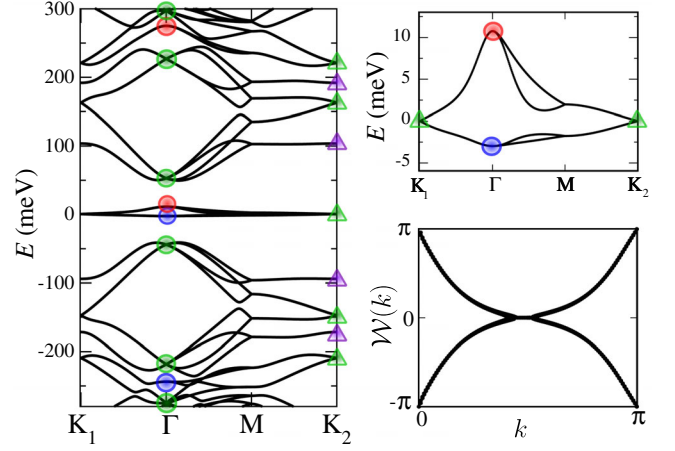

FIG. 2. (a) Electronic band structure of twisted bilayer graphene at the angle $\theta = 1.08$ after full atomic relaxation. The charge neutrality point is the zero of energy. The irreps at the $\mathbf{\Gamma}$ point are encoded by colored circles, where blue, red, and green stand for the $A_1 + B_1$, $A_2 + B_2$, and $E_1 + E_2$ irreps of the D_6 space group, respectively. At the $\mathbf{K}_2$ point the E and $A_1 + A_2$ irreps of the little group D_3 are represented by green and violet triangles, respectively. (b) Enlargement of the FBs region. (c) Wilson loop of the four FBs as function of $k = G_2/\pi$.

relaxed atomic positions, using hopping amplitudes tuned to reproduce *ab initio* calculations [5]. The colored circles and triangles at the $\mathbf{\Gamma}$ and $\mathbf{K}$ points, respectively, indicate the irreps that transform like the corresponding Bloch states. For instance, at $\mathbf{\Gamma}$ the FBs consist of two doublets, the lower corresponding to the irreps $A_1 + B_1$, and the upper to $A_2 + B_2$. Right above and below the FBs, we find at $\mathbf{\Gamma}$ two quartets, each transforming like $E_1 + E_2$. At $\mathbf{K}$, the FBs are degenerate and form a quartet $E + E$. Consistently with the D_3 little group containing C_{3z} and C_{2y}, at $\mathbf{K}$ we find either quartets, like at the FBs, made of degenerate pairs of doublets, each transforming like E, or doublets transforming like $A_1 + A_2$, where A_1 and A_2 differ in the parity under C_{2y}. This overall doubling of degeneracies beyond their expected D_6 space group irreps reflects the valley $U_v(1)$ symmetry of FBs that will be discussed below, and whose eventual breaking will be addressed later in this paper. We end by remarking that the so-called "fragile" topology [13,22,35,46], diagnosed by the odd winding of the Wilson loop [13], is actually robust against lattice corrugations [45] and relaxation, as shown by Fig. 2(c).

A. SU(2) symmetry and accidental degeneracy along C_{2y}-invariant lines

We note that along all directions that are invariant under C_{2y}, which include the diagonals as well as all the edges of the MBZ, the electronic bands show a twofold degeneracy between Bloch states that transform differently under C_{2y}. These lines correspond to the domain walls in real space.

This "accidental" degeneracy is a consequence of the interplay between $U_v(1)$ and C_{2y} symmetries. Indeed, along $\Gamma \to K_{1,2}$ and $M \to K_{1,2}$ in the MBZ we have that

$$C_{2y}(\Psi_{k\sigma}) = \sigma_1\tau_1\mu_3\Psi_{k\sigma}, \qquad (8)$$

and similarly for $\Phi_{k\sigma}$. It follows that the generator of $U_v(1)$, i.e., the operator $\sigma_0\tau_3\mu_0$, anticommutes with the expression of C_{2y} along the lines invariant under that same symmetry, namely the operator $\sigma_1\tau_1\mu_3$, and both commute with the Hamiltonian. Then also their product, $\sigma_1\tau_2\mu_3$, commutes with the Hamiltonian and anticommutes with the other two. The three operators,

$$2T_3 = \sigma_0\tau_3\mu_0, \quad 2T_1 = \sigma_1\tau_1\mu_3, \quad 2T_2 = \sigma_1\tau_2\mu_3, \quad (9)$$

thus realize an SU(2) algebra and all commute with the Hamiltonian $\hat{H}_k$ in momentum space for any C_{2y}-invariant k point. This emergent SU(2) symmetry is therefore responsible for the degeneracy of eigenstates with opposite parity under C_{2y}. We note that C_{2x} instead commutes with $U_v(1)$, so that there is no SU(2) symmetry protection against valley splitting along C_{2x}-invariant lines ($\Gamma \to M$).

IV. PHONONS IN TWISTED BILAYER GRAPHENE

The $U_v(1)$ valley symmetry is an emergent one since, despite the fact that its generator (1) does not commute with the Hamiltonian, the spectrum around charge neutrality is nonetheless $U_v(1)$ invariant. It is therefore not obvious to envisage a mechanism that could efficiently break it.

However, since the lattice d.o.f. play an important role at equilibrium, as discussed in Sec. III, it is possible that they could offer the means to destroy the $U_v(1)$ valley symmetry. In this section, we show that they indeed provide such a symmetry-breaking tool.

A. Valley splitting lattice modulation: The key role of the domain walls

In Sec. II A, we mentioned that the valley symmetry arises because, even though inequivalent Dirac nodes of the two layers should be coupled to each other by the Hamiltonian after being folded onto the same point of the MBZ (see bottom panel in Fig. 1), at small angle these matrix elements are vanishingly small and thus the valleys are effectively decoupled. That is true if the carbon lattice, although mechanically relaxed, is unperturbed by the presence of the electrons. Once coupling with electrons is considered, we cannot exclude that, for example, a lattice distortion modulated with the wave vectors connecting the inequivalent Dirac nodes of the two layers, K_+ with K'_- and K'_+ with K_- in Fig. 1, might instead yield a significant matrix element among the valleys. To investigate that possibility we build an *ad hoc* distortion into the bilayer carbon atom positions. We define the vector $q_{ij} = K_{+,i} - K'_{-,j}$, where

$i, j = 1, 2, 3$ run over the three equivalent Dirac points of the BZ of each layer, and the D_6 conserving displacement field,

$$\eta(r) = \sum_a \sum_{i,j=1}^3 \sin(q_{ij} \cdot r_a) u_{a,ij}\delta(r - r_a), \quad (10)$$

where a runs over all atomic positions, and $u_{a,ij}$ corresponds to a displacement of atom a in direction q_{ij}, whose (tunable) magnitude is the same for all atoms. In proximity of the AA regions the distortion is locally similar to the graphene breathing mode, the in-plane transverse-optical phonon at K [47] with A_1 symmetry. Since by construction q_{ij} is a multiple integer of the reciprocal lattice vectors, $\eta(r)$ has the same periodicity of the unit cell; i.e., the distortion is actually at the Γ point. Moreover, the distortion's D_6 invariance implies no change of space group symmetries. Since the most direct evidence of the $U_v(1)$ symmetry is the accidental degeneracy in the band structure along all C_{2y}-invariant lines, corresponding just to the DWs' directions in real space, we further assume the action of the displacement field $\eta(r)$ to be restricted to a small region in proximity of the DWs,
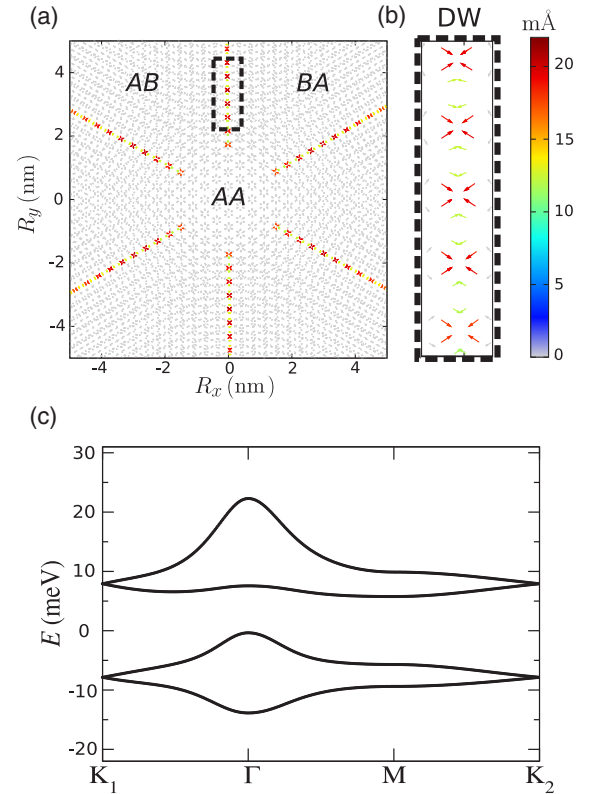

FIG. 3. (a) The displacement field $\eta(r)$, Eq. (10), restricted on the DWs: the direction of the atomic displacement is depicted by a small arrow, while its magnitude in mÅ is expressed in colors. (b) Displacement along the DW area highlighted by a black dashed line in (a). The overall effect of the distortion is a narrowing of the DW. (c) Low-energy band structure of TBLG at $\theta = 1.08$ after the distortion in (a). The twofold degeneracies protected by the valley symmetry are completely lifted.

affecting only $\approx 1\%$ of the atoms in the moiré supercell; see top panels in Fig. 3. The modified FBs in the presence of the displacement field $\boldsymbol{\eta}(\mathbf{r})$ with $|\mathbf{u}_{a,ij}| = 20$ mÅ are shown in the bottom panel of Fig. 3. Remarkably, despite the minute distortion magnitude and the distortion involving only the minority of carbon atoms in the DWs, the degeneracy along $\boldsymbol{\Gamma} \to \mathbf{K}_1$ and $\mathbf{M} \to \mathbf{K}_2$ is lifted to such an extent that the four bands split into two similar copies. This is remarkable in two aspects. First, we repeat, because there is no space symmetry breaking. The only symmetry affected by the distortion is $U_v(1)$, since, by construction, $\boldsymbol{\eta}(\mathbf{r})$ preserve the full space group symmetries. Second, the large splitting magnitude reflects an enormous strength of the effective electron-phonon coupling, whose origin is interesting. Generally speaking, in fact, broad bands involve large hoppings and large absolute electron-phonon couplings, while the opposite is expected for narrow bands. The large electron-phonon couplings which we find for the low-energy bands of TBLG suggest a possible broadband origin of the FBs, as we discuss in Sec. VII. A consequence of this e-ph coupling magnitude is that all potential phenomena involving lattice distortions, either static or dynamic, should be considered with a much larger priority than done so far.

B. Phonon spectrum

We compute the phonon eigenmodes in the relaxed bilayer structure by standard methods; see Appendix A for details of the calculation. Figure 4 shows the phonon density of states $F(\omega)$ for TBLG at three different twist angles in comparison with the Bernal AB-stacked bilayer. As previously reported [28,48], $F(\omega)$ is almost independent of the twist angle, which only affects the interlayer van der Waals forces, much weaker than the in-plane ones arising from the stiff C–C bonds. As a consequence, phonons in TBLG are basically those of the Bernal-stacked bilayer. This is true except for a small set of special phonon

modes, clearly distinguishable in Fig. 5 that depicts the phonon spectrum enlarged in a very narrow energy region ≈ 0.04 meV around the high-frequency graphene $\mathbf{K}$-point peak of the phonon density of states. Specifically, within the large number of energy levels of all other highly dispersive phonon bands, unresolved in the narrow energy window, a set of 10 almost dispersionless modes emerges. We note that these special modes show the same accidental degeneracy doubling along the C_{2y}-invariant lines as that of the electronic bands around the charge neutrality point.

Similar to the electronic degeneracy, whose underlying $U_v(1)$ symmetry arises from vanishingly weak hopping matrix elements between interlayer $\mathbf{K}$-$\mathbf{K}'$ points in the Hamiltonian, the mechanically weak van der Waals interlayer coupling here leads to an effective $U_v(1)$ symmetry for this group of lattice vibrations. Their poor dispersion is connected with a displacement which is nonuniform in the supercell, and is strongly modulated on the moiré length scale, a distinctive feature of these special modes that we denote as "moiré phonons." In particular, it is maximum in the center of the AA zones, finite in the DWs, and negligible in the large AB and BA Bernal regions. The overlap between the displacement $\boldsymbol{\eta}(\mathbf{r})$ in Eq. (10) and the 33 492 phonons of the $\theta = 1.08$ TBLG at the $\boldsymbol{\Gamma}$ point is non-negligible only for those moiré phonons. In particular, we find the highest overlap with the doubly degenerate mode marked by a red arrow in Fig. 5, and which transforms like $A_1 + B_1$. In Fig. 6(a), we show the real space

FIG. 5. Enlargement of the optical region of the phonon spectrum of the fully relaxed TBLG at $\theta = 1.08$. Among many scattered energy levels of highly dispersive branches (not resolved in this narrow energy window), a set of 10 narrow continuous branches stands out (no line drawn through data points, which just fall next to one another). The degeneracy of these modes is twice that expected by D_6 space symmetry, similar in this to electronic bands. The twofold degenerate mode with the highest overlap with the deformation $\boldsymbol{\eta}(\mathbf{r})$, drawn in Fig. 6, is marked by a red arrow, while the mode at $\mathbf{M}$ used in Sec. VI is marked by a green arrow. The avoided crossing which occurs close to $\boldsymbol{\Gamma}$ is encircled by a blue dashed line.
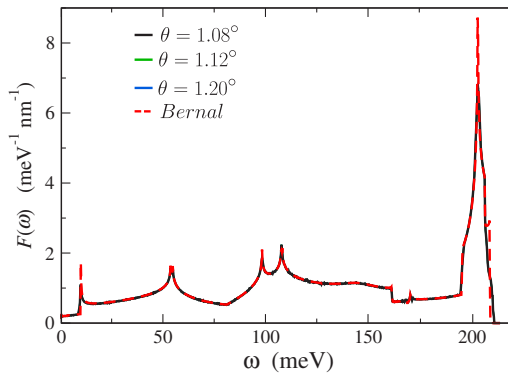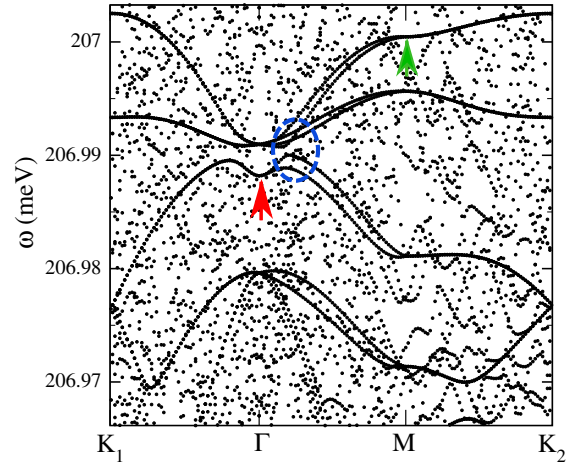

FIG. 4. Phonon density of states $F(\omega)$ for Bernal-stacked bilayer graphene at zero twist angle (red dashed line) and fully relaxed TBLG at $\theta = 1.20, 1.12, 1.08$ (blue, green, and black lines).
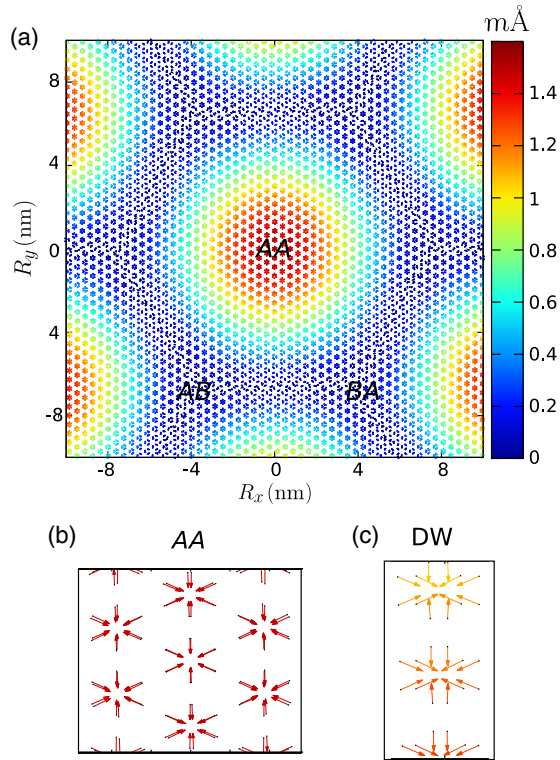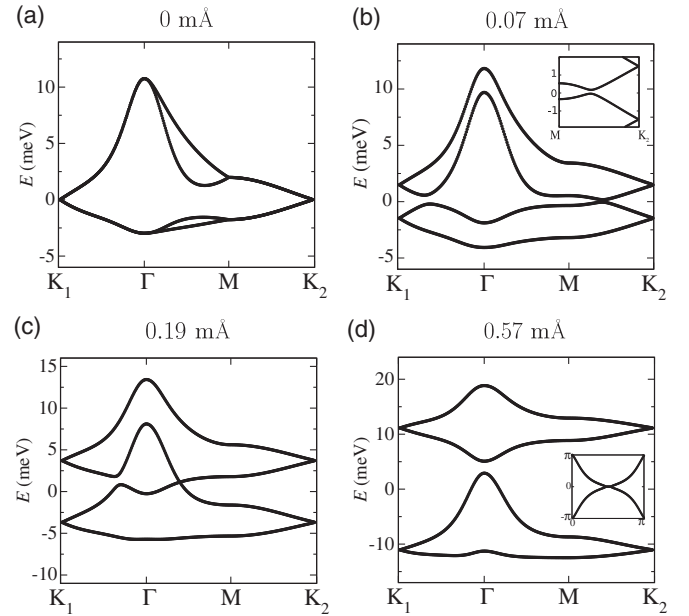
FIG. 6.   (a) Atomic displacements on one of the two layers corresponding to the A_1 symmetry moiré mode of the phonon doublet marked by a red arrow in Fig. 5. The direction of displacement is represented by a small arrow centered at each atomic position, while its modulus is encoded in colors. The mean displacement per atom is 0.57 mÅ. (b) Enlargement of the center of an AA region, shown for both layers. (c) Enlargement along one of the domain walls. Note the similarity with the *ad hoc* displacement in Fig. 3.

distortion corresponding to the A_1 component of the doublet, where the displacement direction is represented by small arrows, while its intensity is encoded in colors. This inspection of the eigenvectors of these modes at the atomistic level reveals a definite underlying single-layer graphene character, specifically that of the A_1 symmetry transverse-optical mode at **K**. Since the graphene **K** point does *not* fold into the bilayer **Γ** point, their appearance along the whole **Γ → K** line in the spectrum of the fully relaxed bilayer must be merely a consequence of relaxation, a relaxation that is particularly strong precisely in the AA and DW regions.

V. INSULATING STATE AT CHARGE NEUTRALITY

We next focus on the effect on the electronic band structure of a carbon atom displacement corresponding to the two degenerate phonon modes A_1 and B_1 at **Γ**, which should affect the valley symmetry as the displacement in Fig. 3. In order to verify that, we carried out a frozen

VIDEO 1.   Evolution of the FBs when the lattice is distorted with increasing intensity along one of the two modes indicated by a red arrow in Fig. 5. (a) Undistorted. (b) Mean displacement per atom 0.07 mÅ. In the inset we show the avoided crossing along **M → K₂**. (c) Mean displacement 0.19 mÅ. Now the avoided crossing appears as a genuine crossing protected by C_{2x} symmetry along **Γ → M**, which actually leads to Dirac points. (d) Mean displacement 0.57 mÅ, opening a gap between the FBs. Inset: Wilson loop of the lowest two bands in (d).

phonon calculation of the modified FB electronic structure with increasing intensity of the deformation (see Video 1). Remarkably, despite transforming as different irreps (A_1 or B_1), both frozen-phonon distortions are not only degenerate, but have exactly the same effect on the bands. As soon as the lattice is distorted, see Video 1(b), the fourfold degeneracy at K_1 and K_2, and the twofold one at **Γ** and **M** is lifted, and small avoided crossings appear and start to move from $K_{1(2)}$ towards the **M** points. Once they cross **M**, they keep moving along **M → Γ**; see Video 1(c). However, along these directions, the C_{2x} symmetry prevents the avoided crossings, and thus leads to six elliptical Dirac cones. Finally, once they reach **Γ** at a threshold value of the distortion, the six Dirac points annihilate so that a gap opens at charge neutrality; see Video 1(d). This gap-opening mechanism is very efficient, with large splittings even for small values of the atomic displacement amplitude shown in Video 1. For instance, an average displacement as small as ≈0.5 mÅ per atom is enough to completely separate the four FBs and to open a gap at charge neutrality.

We emphasize that this occurs without breaking any spatial symmetry of the TBLG, just $U_v(1)$. As a consequence, the insulator state possesses a nontrivial topology, as highlighted by the odd winding of the Wilson loop of the

lowest two bands, shown in the inset of Video 1(d). In turn, the nontrivial topology of the system implies the existence of edge states within the gap separating the two lower flatbands from the two upper ones. We thus recalculated the band structure freezing the moiré phonon with A_1 symmetry at Γ in a ribbon geometry, which is obtained by cutting the TBLG along two parallel domain walls in the y direction at a distance of 7 supercells. The ribbon has therefore translational symmetry along y, but it is confined in the x direction. In Fig. 7, we show the single-particle energy levels as a function of the momentum k_y along the y direction. Edge states within the gap at charge neutrality are clearly visible. In particular, we find for each edge two counterpropagating modes.

As a matter of fact, recent experiments do report the existence of a finite gap also at charge neutrality [4,49], which is actually bigger than at other nonzero integer fillings, and appears without a manifest breakdown of time-reversal symmetry T [4] or C_{2z} symmetry [49], and with the FBs still well separated from other bands [49]. These evidences seem not to support an interaction-driven gap, which would entail either T or TC_{2z} symmetry breakings [4,50], or else the FBs touching other bands at the Γ point [4]. Our phonon-driven insulator at charge neutrality breaks instead $U_v(1)$ and, eventually, C_{2y} and C_{2z} if the frozen phonon has B_1 character, which are symmetries experimentally elusive. However, the edge states that we predict could be detectable by STM or scanning tunneling
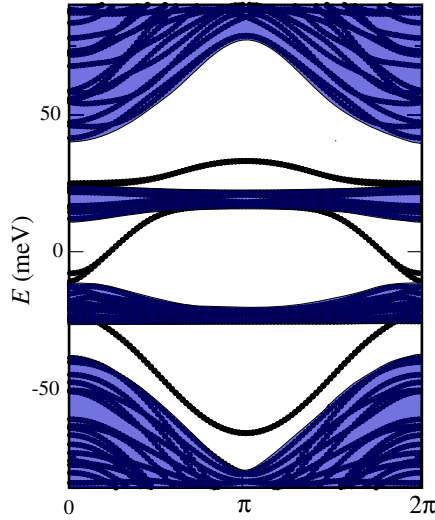

FIG. 7.   The band structure of twisted bilayer graphene at $\theta \approx 1.08°$ in a ribbon geometry with open boundary conditions. The atomic structure inside the unit cell (replicated 7 times along the x direction) has been deformed with the A_1-symmetric moiré phonon mode. With a mean deformation amplitude of ≈ 1.14 m Å, that mode is so strongly coupled to open a large electronic gap at charge neutrality point of ≈ 25 meV. The bulk bands have been highlighted in blue to emphasize the presence of edge states both within the phonon-driven FBs gap and the gaps above and below them.

spectroscopy, thus providing support or disproving the mechanism that we uncovered.

We end by mentioning that near charge neutrality there is compelling evidence of a substantial breakdown of C_{3z} symmetry [16,17,49]. Although that is not expected to stabilize on its own an insulating gap unless the latter were in fact just a pseudogap [50], this symmetry breaking needs a specific discussion, which we will give in Sec. VI A.

A. $E \otimes e$ Jahn-Teller effect

The evidence that the two degenerate modes marked by a red arrow in Fig. 5 produce the same band structure in a frozen-phonon distortion is reminiscent of a $E \otimes e$ Jahn-Teller effect, i.e., the coupling of a doubly degenerate vibration with a doubly degenerate electronic state [31].

Let us consider the action of the two Γ-point A_1 and B_1 phonon modes, hereafter denoted as q_1 and q_2, along the C_{2y}-invariant lines. We note that the A_1 mode, q_1, although invariant under the D_6 group elements, is able to split the degeneracy along those lines. Therefore, it must be coupled to the electrons through a D_6 invariant operator that does not commute with the $U_v(1)$ generator τ_3. That in turn cannot but coincide with C_{2y} itself, which, along the invariant lines, is the operator $T_1 = \sigma_1\tau_1\mu_3/2$ in Eq. (9). On the other hand, the B_1 mode, q_2, is odd under C_{2y}, and thus it must be associated with an operator that anticommutes with C_{2y} and does not commute with τ_3. The only possibility that still admits a U(1) valley symmetry is the operator $T_2 = \sigma_1\tau_2\mu_3/2$ in Eq. (9). Indeed, with such a choice, the electron-phonon Hamiltonian is

$$H_{e\text{-ph}} = -g(q_1 T_1 + q_2 T_2), \tag{11}$$

with g the coupling constant. This commutes with the operator

$$J_3 = T_3 + L_3 = \frac{\tau_3}{2} + \mathbf{q} \wedge \mathbf{p} \tag{12}$$

[where $\mathbf{p} = (p_1, p_2)$ is the conjugate variable of the displacement $\mathbf{q} = (q_1, q_2)$], the generator of a generalized $U_v(1)$ symmetry that involves electron and phonon variables. As anticipated, the Hamiltonian (11) describes precisely a $E \otimes e$ Jahn-Teller problem [31,51,52].

Since the phonon mode $\mathbf{q}$ is almost dispersionless, see Fig. 5, we can think of it as the vibration of a moiré supercell, as if the latter were a single, though very large, molecule, and the TBLG a molecular conductor. In this language, the band structures shown in Video 1 would correspond to a static Jahn-Teller distortion. However, since the phonon frequency is substantially larger than the width of the flatbands, we cannot exclude the possibility of a dynamical Jahn-Teller effect that could mediate superconductivity [51,53], or even stabilize a Jahn-Teller Mott insulator [52] in the presence of a strong enough interaction.

The Jahn-Teller nature of the electron-phonon coupling entails a very efficient mechanism to split the accidental degeneracy, linear in the displacement within a frozen-phonon calculation. However, this does not explain why an in-plane displacement as small as 0.57 mÅ is able to split the formerly degenerate states at Γ by an amount as large as 15 meV, see Video 1(d), of the same order as the original width of the flatbands. To clarify that, we note that this displacement would yield a change in the graphene nearest-neighbor hopping of around $\delta t \simeq 3.6$ meV, see Eq. (A1), which in turn entails a splitting at Γ of $6\delta t \sim 21$ meV, close to what we observe. We believe that such correspondence is not accidental, but indicates that the actual energy scale underneath the flatbands is on the order of the bare graphene bandwidth, rather than the flat bandwidth itself. We return to this issue later in Sec. VII.

VI. INSULATING STATES AT OTHER COMMENSURATE FILLINGS

The Γ-point distortion described above can lead to an insulating state at charge neutrality, possibly connected with the insulating state very recently reported [4,49]. The same phonon branch might also stabilize insulating states at other integer occupancies of the mini bands besides charge neutrality. However, this necessarily requires freezing a mode at a high-symmetry $\mathbf{k}$ point different from Γ in order to get rid of the band touching at the Dirac points, $\mathbf{K}_1$ and $\mathbf{K}_2$, protected by the C_{6z} symmetry. We consider one of the two degenerate phonon modes at the $\mathbf{M}$ point marked by a green arrow in Fig. 5. This mode has similar features to the Jahn-Teller one at Γ, even if it belongs to an upper branch due to an avoided crossing along $\Gamma \to \mathbf{M}$ (blue dashed line in Fig. 5). In Fig. 8, we depict this mode, which still transforms as the A_1 of the graphene $\mathbf{K}$ point on the microscopic graphene scale, but whose long-wavelength modulation now forms a series of ellipses elongated along some of the DWs, thus macroscopically breaking the C_{3z} symmetry of the moiré superlattice.

In Fig. 9, we show the DOS of the FBs obtained by a frozen-phonon realistic tight-binding calculation. Besides the band gaps at $\nu = \pm 4$, which separate the FBs from the other bands, now small gaps open at $\nu = \pm 2$ with an average atomic displacement of 1.8 mÅ induced by the mode at $\mathbf{M}$.

Finally, we also considered a more exotic multi-component distortion induced by a combination of the modes at the three inequivalent $\mathbf{M}$ points, which quadruples the unit cell (see Fig. 10). The resulting DOS of the FBs is shown in Fig. 11 and displays small gaps at the odd integer occupancies $\nu = 1$ and $\nu = \pm 3$.

The very qualitative conclusion of this exploration is that frozen-phonon distortions with various $\mathbf{k}$ vectors can very effectively yield Peierls-like insulating states at integer hole or electron fillings. Of course, all distortions at $\mathbf{k}$ points different from Γ also represent super-superlattices, with an enlargement of the unit cell that should be verifiable
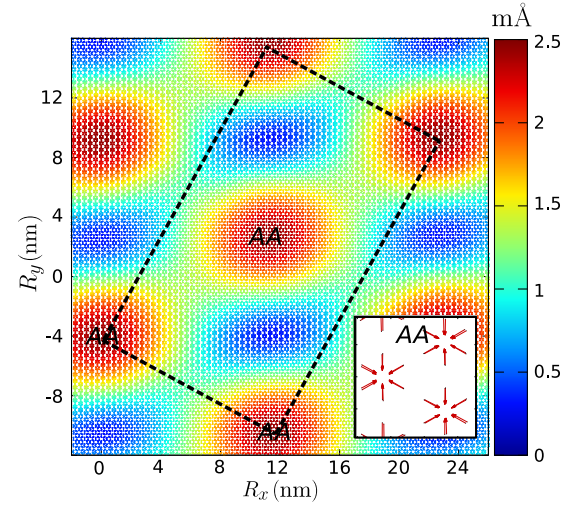

FIG. 8. Atomic displacements on one of the two layers corresponding to one of the moiré modes at $\mathbf{M}$ marked by a green arrow in Fig. 5. The direction of displacement is represented by a small arrow centered at each atomic position, while its modulus is encoded in colors. The mean deformation is 1.8 mÅ and leads to the DOS in Fig. 9. The inset shows an enlargement of the AA region close to the origin. The rectangular unit cell, now containing twice the number of atoms, is highlighted by a black dashed line.

in such a Peierls state, even if the displacement is a tiny fraction of the equilibrium C–C distance. We note here that the zone boundary phonons are less effective in opening gaps at nonzero integer fillings than the zone center phonons are at the charge neutrality point. The reason is that away from charge neutrality the Jahn-Teller effect alone is no longer sufficient; one needs to invoke zone
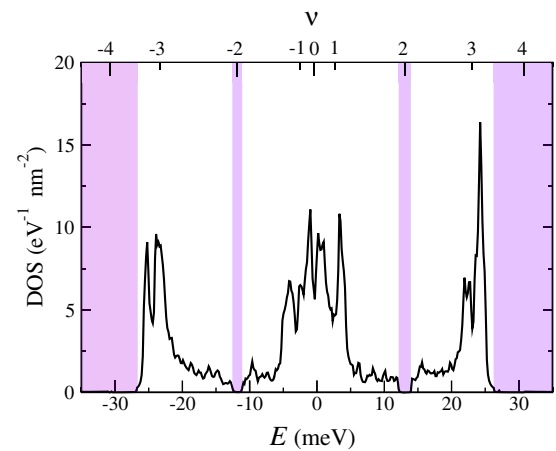

FIG. 9. Density of states in the flatbands region after the TBLG has been distorted by one of the two degenerate modes at $\mathbf{M}$ marked by a green arrow in Fig. 5. A mesh of 40×40 points in the MBZ has been used. The DOS is expressed as function of energy, the zero corresponding to the charge neutrality point, and corresponding occupancy ν of the FBs. The band gaps at $\nu = \pm 2, \pm 4$ are highlighted in violet. The mean displacement per atom is 1.8 mÅ.
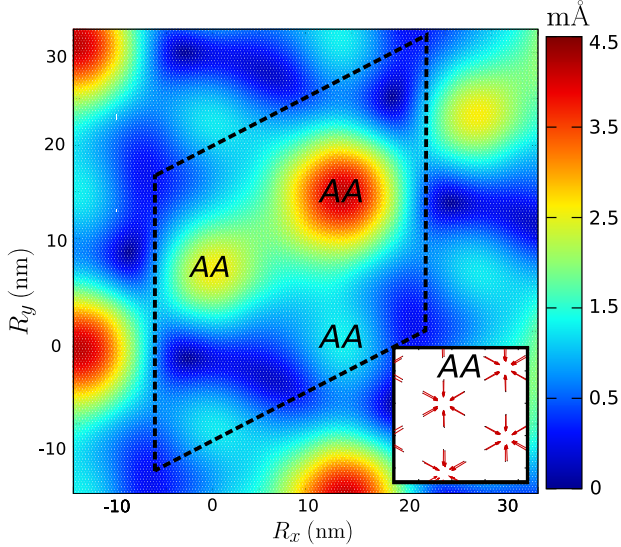
FIG. 10. Atomic displacements on one of the two layers corresponding to multicomponent deformation obtained combining moiré JT phonons at three inequivalent **M** points. The mean deformation is 1.7 mÅ and leads to the DOS in Fig. 11. The intensity of displacement is encoded in colors. The inset shows an enlargement of one of the AA regions when both layers are considered. The unit cell, denoted by a black dashed line, is 4 times larger than the original one.
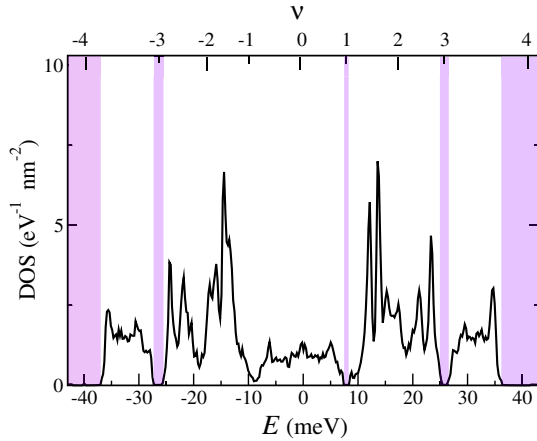

FIG. 11. Electronic density of states with a multicomponent lattice distortion obtained by freezing a combination of the modes at the three inequivalent **M** points. Band gaps at $\nu = +1, \pm3, \pm4$ are highlighted in violet. The mean displacement per atom is 1.7 mÅ.

boundary phonons that enlarge the unit cell, and thus open gaps at the boundaries of the folded Brillouin zone. The efficiency of such a gap-opening mechanism is evidently lower than that of the Jahn-Teller **Γ**-point mode.

A. C_{3z} symmetry breaking

We observe that the multicomponent distortion with the phonons frozen at the inequivalent **M** points leads to a

width of the FBs 5 times larger than in the undistorted case, see Fig. 11 as opposed to Video 1(a), which is not simply a consequence of the tiny gaps that open at the boundary of the reduced Brillouin zone. Such a substantial bandwidth increase suggests that the TBLG may be intrinsically unstable to C_{3z} symmetry breaking, especially near charge neutrality. Electron-electron interaction treated in the mean field does a very similar job [17]. Essentially, both interaction- and phonon-driven mechanisms act right in the same manner: they move the two van Hove singularities of the fully symmetric band structure away from each other, and split them into two, with the net effect of increasing the bandwidth. As such, those two mechanisms will cooperate to drive the C_{3z} symmetry breaking, or enhance it when explicitly broken by strain, not in disagreement with experiments [16,17,49]. The main difference is that the moiré phonons also break $U_v(1)$, and thus are able to open gaps at commensurate fillings that C_{3z} symmetry breaking alone would not do.

VII. PHONON-MEDIATED SUPERCONDUCTIVITY

Here we indicate how the phenomena described above can connect to a superconducting state mediated by electron-phonon coupling. For that, we need to build a minimal tight-binding model containing a limited set of orbitals. For the sake of simplicity, we shall not require the model Hamiltonian to reproduce precisely the shape of all the bands around charge neutrality, especially those above or below the FBs, but only the correct elementary band representation, topology, and, obviously, the existence of the four flatbands separated from all the others. Considering, for instance, only the 32 states at **Γ** closest to the charge neutrality point, and maintaining our assumption of WOs centered at the Wyckoff positions $2c$, those states (apart from avoided crossings allowed by symmetry) would evolve from **Γ** to $\mathbf{K}_1$ in accordance with the D_6 space group as shown in Fig. 12. Once we allow same-symmetry Bloch states to repel each other along $\mathbf{\Gamma} \to \mathbf{K}_1$, the band representation can look similar to the real one (Fig. 2), including the existence of the four FBs that start at **Γ** as two doublets, $A_1 + B_1$ and $A_2 + B_2$, and end at $\mathbf{K}_1$ as two degenerate doublets, each transforming as the 2D irrep E; see the two solid black lines in Fig. 12. While this picture looks compatible with the actual band structure, we shall take a further simplification and just consider the thicker red, blue, and green bands in Fig. 12, which could still produce flatbands with the correct symmetries. This oversimplification obviously implies giving up the possibility to accurately reproduce the shape of the FBs—but it makes the algebra much simpler.

Within this approximation the components of the spinor operators in Eq. (2) are actually single fermionic operators, so that we limit ourselves to just four WOs for each sublattice, AB or BA, and valley, 1 and 2. Two of such WOs
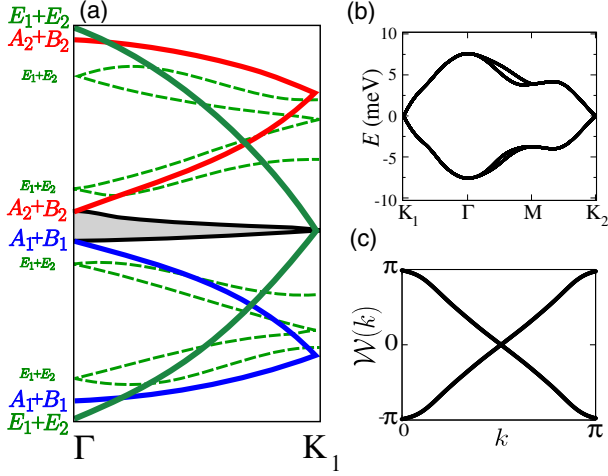
FIG. 12. (a) Sketch of the elementary band representation along $\Gamma \rightarrow \mathbf{K}_1$ taking into account the 32 bands closest to the charge neutrality point and without allowing avoided crossing between same-symmetry Bloch states. Blue, red, and green lines refer to Bloch states that at Γ transform like $A_1 + B_1$, $A_2 + B_2$, and $E_1 + E_2$, respectively. Should we allow for avoided crossings, close to charge neutrality we would obtain the four flatbands shown as black lines surrounding the shaded region. (b) The FBs obtained by a model tight-binding Hamiltonian that includes only the solid bands of (a). The details of this Hamiltonian are given in Appendix B. (c) Wilson loop corresponding to the four bands in (b) fully occupied.

transform like the 1D irreps, one even, A_1, and the other odd, A_2, under C_{2x}. The other two instead transform like the 2D irrep E. We build a minimal tight-binding model,

$$H_e = -\Delta \sum_{\mathbf{R}\sigma} \Psi_{\mathbf{R}\sigma}^{\dagger} \sigma_0 \tau_0 \mu_3 \Psi_{\mathbf{R}\sigma} + T_e, \qquad (13)$$

where Δ splits the s from the p WOs of the 1D irreps, and T_e includes first- and second-neighbor hopping between AB and BA regions in the moiré superlattice compatible with all symmetries; see Appendix B for details. In Fig. 12, we show the resulting FBs as well as their Wilson loop. We emphasize that the FBs arise in this picture from a sequence of avoided crossings between a large set of relatively broad bands that strongly repel each other away from the high-symmetry points, rather than from truly localized WOs. This mechanism is also compatible with, and in fact behind, the strong electron-phonon coupling strength, and the consequently large effects on the FBs of the Jahn-Teller phonons that, according to Eq. (11), simply modulate the AB-BA hopping.

A. Mean-field superconducting state

Neglecting the extremely small dispersion of the moiré Jahn-Teller phonons, we can write their Hamiltonian simply as

$$H_{\mathrm{ph}} = \frac{\omega}{2} \sum_{\mathbf{R}} (\mathbf{p}_{\mathbf{R}} \cdot \mathbf{p}_{\mathbf{R}} + \mathbf{q}_{\mathbf{R}} \cdot \mathbf{q}_{\mathbf{R}}), \qquad (14)$$

with $\omega \simeq 207$ meV.

Rather than trying to model more faithfully the Jahn-Teller coupling (11), we follow a simplified approach based just on symmetry considerations.

In general, we could integrate out the phonons to obtain a retarded electron-electron attraction that can mediate superconductivity. However, since here the phonon frequency is much larger that the bandwidth of the FBs, where the chemical potential lies, we can safely neglect retardation effects making a BCS-type approximation virtually exact. The attraction thus becomes instantaneous and can be represented as in Fig. 13. The phonon couples electrons in nearest-neighbor AB and BA regions, giving rise to an intermoiré site spin-singlet pairing, a state which we expect to be much less affected by Coulomb repulsion than an on-site one. Therefore, neglecting Coulomb repulsions we can concentrate on the pairing channel between nearest-neighbor AB and BA regions. The scattering processes in Fig. 13 imply that the pairing channels are only $\tau_1\mu_0$ and $\tau_1\mu_3$, corresponding to intervalley pairing, as expected because time reversal interchanges the two valleys.

Having assumed pairing between nearest-neighbor AB and BA regions, we must identify pair functions in momentum space that connect nearest-neighbor unit cells, and transform properly under C_{3z}. These functions are

$$\gamma(\mathbf{k}) = e^{i\mathbf{k}\cdot(\mathbf{a}+\mathbf{b})/3}(1 + e^{-i\mathbf{k}\cdot\mathbf{a}} + e^{-i\mathbf{k}\cdot\mathbf{b}}),$$
$$\gamma_{+1}(\mathbf{k}) = e^{i\mathbf{k}\cdot(\mathbf{a}+\mathbf{b})/3}(1 + \omega e^{-i\mathbf{k}\cdot\mathbf{a}} + \omega^* e^{-i\mathbf{k}\cdot\mathbf{b}}),$$
$$\gamma_{-1}(\mathbf{k}) = e^{i\mathbf{k}\cdot(\mathbf{a}+\mathbf{b})/3}(1 + \omega^* e^{-i\mathbf{k}\cdot\mathbf{a}} + \omega e^{-i\mathbf{k}\cdot\mathbf{b}}), \qquad (15)$$

where $\omega = e^{i2\pi/3}$. Specifically, $\gamma(\mathbf{k}) \sim A_1$ is invariant under C_{3z}, while

$$\gamma_{\pm 1}(C_{3z}(\mathbf{k})) = \omega^{\pm 1}\gamma_{\pm 1}(\mathbf{k}). \qquad (16)$$

In other words, $(\gamma_{+1}(\mathbf{k}), \gamma_{-1}(\mathbf{k}))$ form a representation of the 2D irrep $E = (E_{+1}, E_{-1})$ in which C_{3z} is diagonal with eigenvalues ω and ω^*.
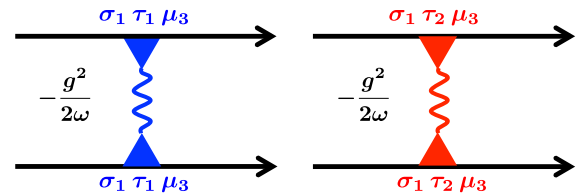

FIG. 13. Phonon-mediated attraction. The two scattering channels corresponds to the two phonons and have the same amplitude $g^2/2\omega$.

Here it is more convenient to transform the spinor $\Phi_{\mathbf{k}\sigma}$,

$$\begin{pmatrix} \Phi_{+1,\mathbf{k}\sigma} \\ \Phi_{-1,\mathbf{k}\sigma} \end{pmatrix} = \frac{1}{\sqrt{2}} \begin{pmatrix} 1 & -i \\ 1 & +i \end{pmatrix} \begin{pmatrix} \Phi_{s,\mathbf{k}\sigma} \\ \Phi_{p,\mathbf{k}\sigma} \end{pmatrix}, \qquad (17)$$

so that $\Phi_{\pm 1,\mathbf{k}\sigma}$ is associated with a WO that transforms like $E_{\pm 1}$. Under the assumption of pairing diagonal in the irreps, we can construct the following spin-singlet Cooper pairs:

$$\sum_{\sigma} \sigma \Phi^{\dagger}_{+1,AB,\mathbf{k}\sigma} \tau_1 \Phi^{\dagger}_{+1,BA,-\mathbf{k}-\sigma} \sim E_{-1,\mathbf{k}}, \qquad (18)$$

$$\sum_{\sigma} \sigma \Phi^{\dagger}_{-1,AB,\mathbf{k}\sigma} \tau_1 \Phi^{\dagger}_{-1,BA,-\mathbf{k}-\sigma} \sim E_{+1,\mathbf{k}}, \qquad (19)$$

$$\frac{1}{\sqrt{2}} \sum_{\sigma} \sigma (\Phi^{\dagger}_{+1,AB,\mathbf{k}\sigma} \tau_1 \Phi^{\dagger}_{-1,BA,-\mathbf{k}-\sigma} \qquad (20)$$

$$+(-)\Phi^{\dagger}_{-1,AB,\mathbf{k}\sigma} \tau_1 \Phi^{\dagger}_{+1,BA,-\mathbf{k}-\sigma}) \sim A_{1(2),\mathbf{k}}, \qquad (21)$$

$$\frac{1}{\sqrt{2}} \sum_{\sigma} \sigma \Psi^{\dagger}_{AB,\mathbf{k}\sigma} \tau_1 \mu_{0(3)} \Psi^{\dagger}_{BA,-\mathbf{k}-\sigma} \sim A'_{1(2),\mathbf{k}}, \qquad (22)$$

which can be combined with the **k**-dependent functions in Eq. (15) to give pair operators that transform like the irreps of D_3. For instance, multiplying Eq. (18) by $\gamma_{+1}(\mathbf{k})$, Eq. (19) by $\gamma_{-1}(\mathbf{k})$, Eq. (21) with the plus sign by $\gamma(\mathbf{k})$, or Eq. (22) with μ_0 by $\gamma(\mathbf{k})$, we obtain pair operators that all transform like A_1. We shall denote their sum as $\mathbf{A}^{\dagger}_{1\mathbf{k}}$, and, similarly, all other symmetry combinations as $\mathbf{A}^{\dagger}_{2\mathbf{k}}$ and $\mathbf{E}^{\dagger}_{\pm 1,\mathbf{k}}$. Evidently, since in our modeling the FBs are made of 1D and 2D irreps, the gap function will in general involve a combination of $\gamma(\mathbf{k})$ and $\gamma_{\pm 1}(\mathbf{k})$; namely, it will be a superposition of s and $d \pm id$ symmetry channels. The dominant channel will depend on which is the prevailing WO character of the Bloch states at the chemical potential, as well as on the strength of the scattering amplitudes in the different pairing channels, $\mathbf{A}^{\dagger}_{1\mathbf{k}}$, $\mathbf{A}^{\dagger}_{2\mathbf{k}}$, and $\mathbf{E}^{\dagger}_{\pm 1,\mathbf{k}}$.

In general, we may expect the totally symmetric A_1 channel to have the largest amplitude; thus we assume the following expression of the phonon-mediated attraction,

$$H_{\text{el-el}} \simeq -\frac{\lambda}{V} \sum_{\mathbf{kp}} \mathbf{A}^{\dagger}_{1\mathbf{k}} \mathbf{A}_{1\mathbf{p}}, \qquad (23)$$

that involves a single parameter $\lambda \sim g^2/2\omega$. We treat the full Hamiltonian (13) plus Eq. (23) in mean field, allowing for a superconducting solution, which is always stabilized by the attraction provided the density of states is finite at the chemical potential. We find that superconductivity opens a gap everywhere in the Brillouin zone. Since
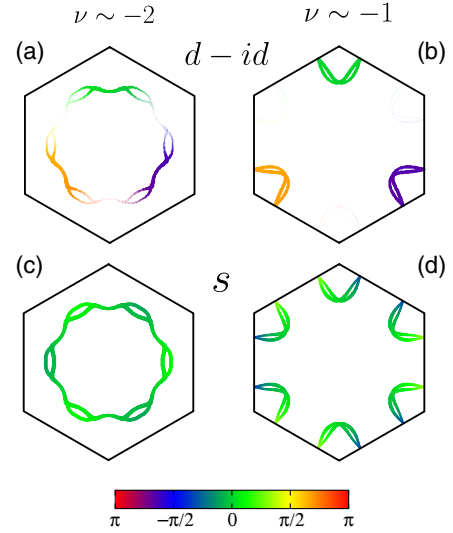

FIG. 14. Pair amplitudes $\Delta(k)^{\dagger}$ of the leading superconducting channels: $d - id$ wave (a),(b) and extended s wave (c),(d). In each panel we show the hexagonal MBZ and the phase amplitudes restricted to a narrow region close to the Fermi surfaces corresponding to the occupancies $\nu \sim -2$ (a),(c) and $\nu \sim -1$ (b),(d). The phase of the superconducting order parameter is expressed in color. Note that the double lines are due to the fact that two bands cross the chemical potential at different **k** points.

$$\langle \mathbf{A}^{\dagger}_{1\mathbf{k}} \rangle = \gamma_{+1}(\mathbf{k}) \langle E_{-1,\mathbf{k}} \rangle + \gamma_{-1}(\mathbf{k}) \langle E_{+1,\mathbf{k}} \rangle + \gamma(\mathbf{k}) \langle A_{1,\mathbf{k}} \rangle$$
$$+ \gamma(\mathbf{k}) \langle A'_{1,\mathbf{k}} \rangle, \qquad (24)$$

the order parameter may have finite components with different symmetries, $E_{\pm 1}$ and A_1. In the model calculation all components acquire similar magnitude, implying a mixture of s- and $d \pm id$-wave symmetries. In Fig. 14, we show $\langle A'_{1,\mathbf{k}} \rangle$ and $\langle E_{-1,\mathbf{k}} \rangle$ at the Fermi surface corresponding to densities $\nu \approx -1$ and $\nu \approx -2$ with respect to charge neutrality. We conclude by emphasizing that the Cooper pair is made by one electron in AB and one in BA, thus leading, in the spin-singlet channel, to extended s and/or $d \pm id$ symmetries. That is merely a consequence of the phonon mode and electron-phonon properties; hence, it does not depend on the above modeling of the FBs.

There are already in the literature several proposals about the superconducting states in TBLG. Most of them, however, invoke electron correlations as the element responsible for or strongly affecting the pairing [22,24,54–71]. There are few exceptions [29,72,73] that instead propose, as we do, a purely phonon-mediated attraction. In Refs. [72,73], the TBLG phonons are assumed to coincide with the single-layer graphene ones, as if the interlayer coupling were ineffective in the phonon spectrum, which is not what we find for the special modes discussed above. Moreover, they both discuss the effects of such phonons only in a continuum model for the FBs. In particular, the authors of Ref. [72]

consider a few selected graphene modes, among which is the transverse-optical mode at **K** that has the largest weight in the TBLG phonon that we consider. They conclude that such graphene mode mediates $d \pm id$ pairing in the A_2 channel, $\tau_1 \mu_3$ in our language, leading to an order parameter odd upon interchanging the two layers. On the contrary, the authors of Ref. [73] focus just on the acoustic phonons of graphene, and conclude they stabilize an extended s-wave order parameter.

VIII. CONCLUSIONS

In this work, we uncovered a novel and strong electron-phonon coupling mechanism and analyzed its potential role in the low-temperature physics of magic angle twisted bilayer graphene, with particular emphasis on the insulating and superconducting states. By working out the phonon modes of a fully relaxed TBLG, we found a special group of a few of them modulated over the whole moiré supercell and nearly dispersionless, thus showing that the moiré pattern can induce flatbands also in the phonon spectrum. In particular, two of these modes, which are degenerate at any **k** point invariant under 180° rotation around the y axis and its C_{3z} equivalent directions, are found to couple strongly to the valley $U_v(1)$ symmetry, that is responsible for the accidental degeneracy of the band structure at the same **k** points where the two modes are degenerate. This particular phonon doublet is strongly Jahn-Teller coupled to the valley d.o.f., realizing a so-called $E \otimes e$ Jahn-Teller model. This mechanism, if static, would generate a filling-dependent broadening of the flatbands and eventually insulating phases at all the commensurate fillings. Interestingly, freezing the modes at $\mathbf{\Gamma}$ can stabilize a topologically nontrivial insulator at charge neutrality that sustains edge modes. We also investigate the symmetry properties of a hypothetical superconducting state stabilized by this Jahn-Teller mode. We find that the phonon-mediated coupling occurs on the moiré scale, favoring spin-singlet pairing of electrons in different Bernal (AB or BA) regions, which may thus condense with an extended s- and/or $d \pm id$-wave order parameter. In a mean-field calculation with a model tight-binding Hamiltonian of the flatbands, we find that the dominant symmetry depends on the orbital character that prevails in the Bloch states at the Fermi energy, as well as on the precise values of scattering amplitudes in the different Cooper channels allowed by the C_{3z} symmetry. We cannot exclude that a nematic component might arise due to higher-order terms not included in our mean-field calculation, as discussed in Refs. [74,75]. These results herald a role of phonons and of lattice distortions of much larger impact than supposed so far in twisted graphene bilayers, which does not exclude a joint action of electron-phonon and electron-electron interaction. Further experimental and theoretical developments will be called for in order to establish their actual importance and role.

APPENDIX A: DETAILS ON THE LATTICE RELAXATION, BAND STRUCTURE, AND PHONON CALCULATIONS

The lattice relaxation and band structure calculation procedures are the same as those thoroughly described in Ref. [10], with the exception that now the carbon-carbon intralayer interactions are modeled via the Tersoff potential [76]. The interlayer interactions are modeled via the Kolmogorov-Crespi (KC) potential [77], using the recent parametrization of Ref. [78]. Geometric optimizations are performed using the FIRE algorithm [79]. The hopping amplitudes of the tight-binding Hamiltonian are

$$t(\mathbf{d}) = V_{pp\sigma}(d) \left[\frac{\mathbf{d} \cdot \mathbf{e}_z}{d} \right]^2 + V_{pp\pi}(d) \left[1 - \left(\frac{\mathbf{d} \cdot \mathbf{e}_z}{d} \right)^2 \right], \quad \text{(A1)}$$

where $\mathbf{d} = \mathbf{r}_i - \mathbf{r}_j$ is the distance between atom i and j, $d = |\mathbf{d}|$, and $\mathbf{e}_z$ is the unit vector in the direction perpendicular to the graphene planes. The out-of-plane (σ) and in-plane (π) transfer integrals are

$$V_{pp\sigma}(x) = V_{pp\sigma}^0 e^{-(x-d_0)/r_0}, \qquad V_{pp\pi}(x) = V_{pp\pi}^0 e^{-(x-a_0)/r_0}, \quad \text{(A2)}$$

where $V_{pp\sigma}^0 = 0.48$ eV and $V_{pp\pi}^0 = -2.8$ eV are values chosen to reproduce *ab initio* dispersion curves in AA and AB stacked bilayer graphene, $d_0 = 3.344$ Å is the starting interlayer distance, $a_0 = 1.3978$ Å is the intralayer carbon-carbon distance obtained with the Tersoff potential, and $r_0 = 0.3187a_0$ is the decay length [5,25].

We compute phonons in TBLG using the force constants of the nonharmonic potentials $U = U_{\text{TERSOFF}} + U_{\text{KC}}$ that we used to relax the structure:

$$C_{\alpha\beta}(il, js) = \frac{\partial^2 U}{\partial R_{\alpha il} \partial R_{\beta js}}, \quad \text{(A3)}$$

where (i, j) label the atoms in the unit cell, (l, s) the moiré lattice vectors, and $\alpha, \beta = x, y, z$. Then, we define the dynamical matrix at phonon momentum **q** as
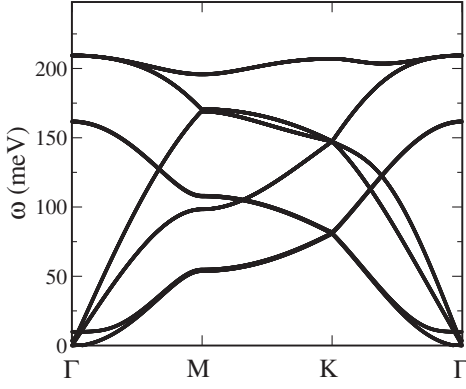
FIG. 15.　Phonon dispersion obtained with our choice of intra-layer and interlayer potentials in Bernal-stacked bilayer graphene.

$$D_{\alpha\beta ij}(\mathbf{q}) = \frac{1}{\mathbf{M}_C}\sum_l C_{\alpha\beta}(il, j0)e^{-i\mathbf{q}R_l}, \qquad (A4)$$

where $\mathbf{M}_C$ is the carbon atom mass. Using the above relation we determine the eigenvalue equation for the normal modes of the system and the phonon spectrum:

$$\sum_{j\beta} D_{\alpha\beta ij}(\mathbf{q})\epsilon_{j\beta}(\mathbf{q}) = \omega_{\mathbf{q}}^2 \epsilon_{i\alpha}(\mathbf{q}), \qquad (A5)$$

where $\omega_{\mathbf{q}}$ denote the energy of the normal mode $\epsilon(\mathbf{q})$. The phonon dispersion of Bernal-stacked bilayer graphene obtained with this method is shown Fig. 15. As can be seen, the transverse-optical (TO) modes at $\mathbf{K}$ are found at $\omega \approx 207$ meV. As a consequence, the Jahn-Teller modes discussed in the main text, which vibrate in the same way on the graphene scale, have similar frequency. However, the frequency of the TO modes in graphene is strongly sensitive to the choice of the intralayer potential used [80], so that these modes can be predicted to have frequencies as low as ≈ 170 meV [81,82]. This implies that also the JT modes may be observed at lower frequency than ours.

APPENDIX B: HAMILTONIAN IN MOMENTUM SPACE

In order to make the invariance under C_{3z} more explicit, we use the transformed spinors,

$$\begin{pmatrix} \Phi_{+1,\mathbf{k}\sigma} \\ \Phi_{-1,\mathbf{k}\sigma} \end{pmatrix} = \frac{1}{\sqrt{2}}\begin{pmatrix} 1 & -i \\ 1 & +i \end{pmatrix}\begin{pmatrix} \Phi_{s,\mathbf{k}\sigma} \\ \Phi_{p,\mathbf{k}\sigma} \end{pmatrix}, \qquad (B1)$$

for the 2D irreps, which correspond to WO eigenstates of C_{3z}. Moreover, it is convenient to also transform the spinors $\Psi_{\mathbf{k}\sigma}$ of the 1D irreps in the same way, i.e.,

$$\begin{pmatrix} \Psi_{+1,\mathbf{k}\sigma} \\ \Psi_{-1,\mathbf{k}\sigma} \end{pmatrix} = \frac{1}{\sqrt{2}}\begin{pmatrix} 1 & -i \\ 1 & +i \end{pmatrix}\begin{pmatrix} \Psi_{s,\mathbf{k}\sigma} \\ \Psi_{p,\mathbf{k}\sigma} \end{pmatrix}, \qquad (B2)$$

which correspond to WOs still invariant under C_{3z} but not under C_{2x}, whose representation both in $\Psi_{\mathbf{k}\sigma}$ and $\Phi_{\mathbf{k}\sigma}$ becomes the Pauli matrix μ_1. In conclusion, the spinor operators defined above satisfy

$$C_{3z}(\Phi_{\mathbf{k}\sigma}) = \begin{pmatrix} \omega & 0 \\ 0 & \omega^* \end{pmatrix}\Phi_{C_{3z}(\mathbf{k})\sigma},$$

$$C_{3z}(\Psi_{\mathbf{k}\sigma}) = \Psi_{C_{3z}(\mathbf{k})\sigma},$$

$$C_{2x}(\Phi_{\mathbf{k}\sigma}) = \mu_1\Phi_{C_{3z}(\mathbf{k})\sigma},$$

$$C_{2x}(\Psi_{\mathbf{k}\sigma}) = \mu_1\Psi_{C_{3z}(\mathbf{k})\sigma}. \qquad (B3)$$

For simplicity, we consider only nearest- and next-nearest-neighbor hopping between WOs centered at different AB and BA regions, which correspond to the following functions in momentum space:

$$\gamma_1(\mathbf{k}) = \alpha_{\mathbf{k}}(1 + e^{-i\mathbf{k}\cdot\mathbf{a}} + e^{-i\mathbf{k}\cdot\mathbf{b}}),$$

$$\gamma_{1,+1}(\mathbf{k}) = \alpha_{\mathbf{k}}(1 + \omega e^{-i\mathbf{k}\cdot\mathbf{a}} + \omega^* e^{-i\mathbf{k}\cdot\mathbf{b}}),$$

$$\gamma_{1,-1}(\mathbf{k}) = \alpha_{\mathbf{k}}(1 + \omega^* e^{-i\mathbf{k}\cdot\mathbf{a}} + \omega e^{-i\mathbf{k}\cdot\mathbf{b}}), \qquad (B4)$$

for first neighbors, and

$$\gamma_2(\mathbf{k}) = \alpha_{\mathbf{k}}(e^{i\mathbf{k}\cdot(\mathbf{a}-\mathbf{b})} + e^{-i\mathbf{k}\cdot(\mathbf{a}-\mathbf{b})} + e^{-i\mathbf{k}\cdot(\mathbf{a}+\mathbf{b})}),$$

$$\gamma_{2,+1}(\mathbf{k}) = \alpha_{\mathbf{k}}(\omega e^{i\mathbf{k}\cdot(\mathbf{a}-\mathbf{b})} + \omega^* e^{-i\mathbf{k}\cdot(\mathbf{a}-\mathbf{b})} + e^{-i\mathbf{k}\cdot(\mathbf{a}+\mathbf{b})}),$$

$$\gamma_{2,-1}(\mathbf{k}) = \alpha_{\mathbf{k}}(\omega^* e^{i\mathbf{k}\cdot(\mathbf{a}-\mathbf{b})} + \omega e^{-i\mathbf{k}\cdot(\mathbf{a}-\mathbf{b})} + e^{-i\mathbf{k}\cdot(\mathbf{a}+\mathbf{b})}),$$

$$(B5)$$

for second neighbors, where $\omega = e^{i2\pi/3}$, $\alpha_{\mathbf{k}} = e^{i\mathbf{k}\cdot(\mathbf{a}+\mathbf{b})/3}$, and the lattice constants $\mathbf{a} = (\sqrt{3}/2, -1/2)$ and $\mathbf{b} = (\sqrt{3}/2, 1/2)$. Since

$$C_{3z}(\mathbf{a}) = \mathbf{b} - \mathbf{a}, \qquad C_{3z}(\mathbf{b}) = -\mathbf{a},$$

$$C_{2x}(\mathbf{a}) = \mathbf{b}, \qquad C_{2x}(\mathbf{b}) = \mathbf{a}, \qquad (B6)$$

then, for $n = 1, 2$,

$$\gamma_n(C_{3z}(\mathbf{k})) = \gamma_n(\mathbf{k}),$$

$$\gamma_{n,\pm 1}(C_{3z}(\mathbf{k})) = \omega^{\pm 1}\gamma_{n,\pm 1}(\mathbf{k}),$$

$$\gamma_n(C_{2x}(\mathbf{k})) = \gamma_n(\mathbf{k}),$$

$$\gamma_{n,\pm 1}(C_{2x}(\mathbf{k})) = \gamma_{n,\mp 1}(\mathbf{k}), \qquad (B7)$$

which shows that $\gamma_{n,\pm 1}(\mathbf{k})$ transform like the 2D irrep E.

We assume the following tight-binding Hamiltonian for the 1D irreps:

$$H_{1D-1D} = \sum_{\mathbf{k}\sigma} \left[-\Delta \Psi^\dagger_{\mathbf{k}\sigma} \sigma_0 \mu_1 \tau_0 \Psi_{\mathbf{k}\sigma} \right.$$
$$\left. - \sum_{n=1,2} t^{(n)}_{11} (\gamma_n(\mathbf{k}) \Psi^\dagger_{\mathbf{k}\sigma} \sigma^+ \mu_0 \tau_0 \Psi_{\mathbf{k}\sigma} + \text{H.c.}) \right], \quad (B8)$$

where $t^{(1)}_{11}$ and $t^{(2)}_{11}$ are the first- and second-neighbor hopping amplitudes, respectively, which we assume to be real.

The 2D irreps have instead the Hamiltonian

$$H_{2D-2D} = -\sum_{\mathbf{k}\sigma} \sum_{n=1}^{2} \left[t^{(n)}_{22} \gamma_n(\mathbf{k}) \Phi^\dagger_{\mathbf{k}\sigma} \sigma^+ \mu_0 \tau_0 \Phi_{\mathbf{k}\sigma} \right.$$
$$\left. + g^{(n)}_{22} \Phi^\dagger_{\mathbf{k}\sigma} \sigma^+ \hat{\gamma}_n(\mathbf{k}) \mu_1 \tau_0 \Phi_{\mathbf{k}\sigma} + \text{H.c.} \right], \quad (B9)$$

with real hopping amplitudes, where

$$\hat{\gamma}_n(\mathbf{k}) = \begin{pmatrix} \gamma_{n,+1}(\mathbf{k}) & 0 \\ 0 & \gamma_{n,-1}(\mathbf{k}) \end{pmatrix}. \quad (B10)$$

Finally, the coupling between 1D and 2D irreps is represented by the Hamiltonian

$$H_{1D-2D} = -\sum_{\mathbf{k}\sigma} \sum_{n=1}^{2} t^{(n)}_{12} [\Phi^\dagger_{\mathbf{k}\sigma} \sigma^+ \mu_1 \hat{\gamma}_n(\mathbf{k}) \mu_1 \tau_0 \Psi_{\mathbf{k}\sigma}$$
$$+ \Psi^\dagger_{\mathbf{k}\sigma} \sigma^+ \hat{\gamma}_n(\mathbf{k}) \tau_0 \Phi_{\mathbf{k}\sigma} + i\Phi^\dagger_{\mathbf{k}\sigma} \sigma^+ \mu_1 \hat{\gamma}_n(\mathbf{k}) \tau_3 \Psi_{\mathbf{k}\sigma}$$
$$+ i\Psi^\dagger_{\mathbf{k}\sigma} \sigma^+ \mu_1 \hat{\gamma}_n(\mathbf{k}) \tau_3 \Phi_{\mathbf{k}\sigma} + \text{H.c.}], \quad (B11)$$

with real $t^{(n)}_{12}$.

The Hamiltonian thus reads

$$H = H_{1D-1D} + H_{2D-2D} + H_{1D-2D}, \quad (B12)$$

which, through Eqs. (B3) and (B7), can be readily shown to be invariant under C_{3z} and C_{2x}, and is evidently also invariant under the $U_v(1)$ generator τ_3. In addition, the Hamiltonian must be also invariant under TC_{2z}, where T is the time-reversal operator. Noting that

$$TC_{2z}(\Phi_{\mathbf{k}\sigma}) = \sigma_1 \mu_1 \Phi_{\mathbf{k}-\sigma},$$
$$TC_{2z}(\Psi_{\mathbf{k}\sigma}) = \sigma_1 \mu_1 \Psi_{\mathbf{k}-\sigma}, \quad (B13)$$

one can show that H in Eq. (B12) is also invariant under that symmetry.

The model Hamiltonian thus depends on eight parameters. The FBs shown in Fig. 12 have been obtained choosing $\Delta = 10$, $t^1_{11} = 2$, $t^1_{22} = 5$, $g^1_{22} = 10$, $t^2_{22} = g^2_{22} = -t^2_{11} = 1.2$, $t^1_{12} = 2$, and $t^2_{12} = 0.5$.

[1] Y. Cao, V. Fatemi, A. Demir, S. Fang, S. L. Tomarken, J. Y. Luo, J. D. Sanchez-Yamagishi, K. Watanabe, T. Taniguchi, E. Kaxiras, R. C. Ashoori, and P. Jarillo-Herrero, *Correlated Insulator Behaviour at Half-Filling in Magic-Angle Graphene Superlattices*, Nature (London) **556**, 80 (2018).

[2] Y. Cao, V. Fatemi, S. Fang, K. Watanabe, T. Taniguchi, E. Kaxiras, and P. Jarillo-Herrero, *Unconventional Superconductivity in Magic-Angle Graphene Superlattices*, Nature (London) **556**, 43 (2018).

[3] M. Yankowitz, S. Chen, H. Polshyn, K. Watanabe, T. Taniguchi, D. Graf, A. F. Young, and C. R. Dean, *Tuning Superconductivity in Twisted Bilayer Graphene*, Science **363**, 1059 (2019).

[4] X. Lu, P. Stepanov, W. Yang, M. Xie, M. A. Aamir, I. Das, C. Urgell, K. Watanabe, T. Taniguchi, G. Zhang, A. Bachtold, A. H. MacDonald, and D. K. Efetov, *Superconductors, Orbital Magnets, and Correlated States in Magic Angle Bilayer Graphene*, arXiv:1903.06513.

[5] G. T. de Laissardiére, D. Mayou, and L. Magaud, *Localization of Dirac Electrons in Rotated Graphene Bilayers*, Nano Lett. **10**, 804 (2010).

[6] G. T. de Laissardière, D. Mayou, and L. Magaud, *Numerical Studies of Confined States in Rotated Bilayers of Graphene*, Phys. Rev. B **86**, 125413 (2012).

[7] S. Shallcross, S. Sharma, E. Kandelaki, and O. A. Pankratov, *Electronic Structure of Turbostratic Graphene*, Phys. Rev. B **81**, 165105 (2010).

[8] A. O. Sboychakov, A. L. Rakhmanov, A. V. Rozhkov, and F. Nori, *Electronic Spectrum of Twisted Bilayer Graphene*, Phys. Rev. B **92**, 075402 (2015).

[9] E. S. Morell, J. D. Correa, P. Vargas, M. Pacheco, and Z. Barticevic, *Flat Bands in Slightly Twisted Bilayer Graphene: Tight-Binding Calculations*, Phys. Rev. B **82**, 121407 (2010).

[10] M. Angeli, D. Mandelli, A. Valli, A. Amaricci, M. Capone, E. Tosatti, and M. Fabrizio, *Emergent D_6 Symmetry in Fully Relaxed Magic-Angle Twisted Bilayer Graphene*, Phys. Rev. B **98**, 235137 (2018).

[11] R. Bistritzer and A. H. MacDonald, *Moiré Bands in Twisted Double-Layer Graphene*, Proc. Natl. Acad. Sci. U.S.A. **108**, 12233 (2011).

[12] G. Tarnopolsky, A. J. Kruchkov, and A. Vishwanath, *Origin of Magic Angles in Twisted Bilayer Graphene*, Phys. Rev. Lett. **122**, 106405 (2019).

[13] Z. Song, Z. Wang, W. Shi, G. Li, C. Fang, and B. A. Bernevig, *All Magic Angles Are Stable Topological*, Phys. Rev. Lett. **123**, 036401 (2019).

[14] P. Lucignano, D. Alfè, V. Cataudella, D. Ninno, and G. Cantele, *Crucial Role of Atomic Corrugation on the Flat Bands and Energy Gaps of Twisted Bilayer Graphene at the Magic Angle $\theta \sim 1.08°$*, Phys. Rev. B **99**, 195419 (2019).

[15] J. Kang and O. Vafek, *Strong Coupling Phases of Partially Filled Twisted Bilayer Graphene Narrow Bands*, Phys. Rev. Lett. **122**, 246401 (2019).

[16] A. Kerelsky, L. McGilly, D. M. Kennes, L. Xian, M. Yankowitz, S. Chen, K. Watanabe, T. Taniguchi, J. Hone, C. Dean, A. Rubio, and A. N. Pasupathy, *Magic Angle Spectroscopy*, Nature (London) **572**, 95 (2019).

[17] Y. Choi, J. Kemmer, Y. Peng, A. Thomson, H. Arora, R. Polski, Y. Zhang, H. Ren, J. Alicea, G. Refael,

F. von Oppen, K. Watanabe, T. Taniguchi, and S. Nadj-Perge, *Imaging Electronic Correlations in Twisted Bilayer Graphene Near the Magic Angle*, arXiv:1901.02997.

[18] H. Polshyn, M. Yankowitz, S. Chen, Y. Zhang, K. Watanabe, T. Taniguchi, C. R. Dean, and A. F. Young, *Phonon Scattering Dominated Electron Transport in Twisted Bilayer Graphene*, arXiv:1902.00763.

[19] Y. Cao, D. Chowdhury, D. Rodan-Legrain, O. Rubies-Bigordà, K. Watanabe, T. Taniguchi, T. Senthil, and P. Jarillo-Herrero, *Strange Metal in Magic-Angle Graphene with Near Planckian Dissipation*, arXiv:1901.03710.

[20] S. L. Tomarken, Y. Cao, A. Demir, K. Watanabe, T. Taniguchi, P. Jarillo-Herrero, and R. C. Ashoori, *Electronic Compressibility of Magic Angle Graphene Superlattices*, Phys. Rev. Lett. **123,** 046601 (2019).

[21] T. O. Wehling, E. Şaşıoğlu, C. Friedrich, A. I. Lichtenstein, M. I. Katsnelson, and S. Blügel, *Strength of Effective Coulomb Interactions in Graphene and Graphite*, Phys. Rev. Lett. **106,** 236805 (2011).

[22] H. C. Po, L. Zou, A. Vishwanath, and T. Senthil, *Origin of Mott Insulating Behavior and Superconductivity in Twisted Bilayer Graphene*, Phys. Rev. X **8,** 031089 (2018).

[23] M. Xie and A. H. MacDonald, *On the Nature of the Correlated Insulator States in Twisted Bilayer Graphene*, arXiv:1812.04213.

[24] Y.-Z. You and A. Vishwanath, *Superconductivity from Valley Fluctuations and Approximate SO(4) Symmetry in a Weak Coupling Theory of Twisted Bilayer Graphene*, arXiv:1805.06867.

[25] N. N. T. Nam and M. Koshino, *Lattice Relaxation and Energy Band Modulation in Twisted Bilayer Graphene*, Phys. Rev. B **96,** 075311 (2017).

[26] S. Carr, S. Fang, P. Jarillo-Herrero, and E. Kaxiras, *Pressure Dependence of the Magic Twist Angle in Graphene Superlattices*, Phys. Rev. B **98,** 085144 (2018).

[27] S. Carr, S. Fang, Z. Zhu, and E. Kaxiras, *Minimal Model for Low-Energy Electronic States of Twisted Bilayer Graphene*, Phys. Rev. Res. **1,** 013001 (2019).

[28] Y. W. Choi and H. J. Choi, *Electron-Phonon Interaction in Magic-Angle Twisted Bilayer Graphene*, Phys. Rev. B **98,** 241412 (2018).

[29] F. Wu, E. Hwang, and S. D. Sarma, *Phonon-Induced Giant Linear-in-T Resistivity in Magic Angle Twisted Bilayer Graphene: Ordinary Strangeness and Exotic Superconductivity*, Phys. Rev. B **99,** 165112 (2019).

[30] I. Yudhistira, N. Chakraborty, G. Sharma, D. Y. H. Ho, E. Laksono, O. P. Sushkov, G. Vignale, and S. Adam, *Gauge Phonon Dominated Resistivity in Twisted Bilayer Graphene Near Magic Angle*, Phys. Rev. B **99,** 140302 (2019).

[31] R. Englman, *The Jahn-Teller Effect in Molecules and Crystals*, in Interscience Monographs and Texts in Physics and Astronomy (Wiley-Interscience, New York, 1972).

[32] L. Rademaker and P. Mellado, *Charge-Transfer Insulation in Twisted Bilayer Graphene*, Phys. Rev. B **98,** 235158 (2018).

[33] L. Zou, H. C. Po, A. Vishwanath, and T. Senthil, *Band Structure of Twisted Bilayer Graphene: Emergent Symmetries, Commensurate Approximants, and Wannier Obstructions*, Phys. Rev. B **98,** 085435 (2018).

[34] J. Kang and O. Vafek, *Symmetry, Maximally Localized Wannier States, and a Low-Energy Model for Twisted Bilayer Graphene Narrow Bands*, Phys. Rev. X **8,** 031088 (2018).

[35] H. C. Po, L. Zou, T. Senthil, and A. Vishwanath, *Faithful Tight-Binding Models and Fragile Topology of Magic-Angle Bilayer Graphene*, Phys. Rev. B **99,** 195455 (2019).

[36] M. Koshino, N. F. Q. Yuan, T. Koretsune, M. Ochi, K. Kuroki, and L. Fu, *Maximally Localized Wannier Orbitals and the Extended Hubbard Model for Twisted Bilayer Graphene*, Phys. Rev. X **8,** 031087 (2018).

[37] N. F. Q. Yuan and L. Fu, *Model for the Metal-Insulator Transition in Graphene Superlattices and Beyond*, Phys. Rev. B **98,** 045103 (2018).

[38] H. Yoo, K. Zhang, R. Engelke, P. Cazeaux, S. H. Sung, R. Hovden, A. W. Tsen, T. Taniguchi, K. Watanabe, G.-C. Yi, M. Kim, M. Luskin, E. B. Tadmor, and P. Kim, *Atomic Reconstruction at van der Waals Interface in Twisted Bilayer Graphene*, Nat. Mater. **18,** 448 (2019).

[39] K. Zhang and E. B. Tadmor, *Structural and Electron Diffraction Scaling of Twisted Graphene Bilayers*, J. Mech. Phys. Solids **112,** 225 (2018).

[40] K. Uchida, S. Furuya, J.-I. Iwata, and A. Oshiyama, *Atomic Corrugation and Electron Localization due to Moiré Patterns in Twisted Bilayer Graphenes*, Phys. Rev. B **90,** 155451 (2014).

[41] S. Dai, Y. Xiang, and D. J. Srolovitz, *Twisted Bilayer Graphene: Moiré with a Twist*, Nano Lett. **16,** 5923 (2016).

[42] S. K. Jain, V. Juričić, and G. T. Barkema, *Structure of Twisted and Buckled Bilayer Graphene*, 2D Mater. **4,** 015018 (2017).

[43] F. Gargiulo and O. V. Yazyev, *Structural and Electronic Transformation in Low-Angle Twisted Bilayer Graphene*, 2D Mater. **5,** 015019 (2018).

[44] F. Guinea and N. R. Walet, *Continuum Models for Twisted Bilayer Graphene: The Effects of Lattice Deformation and Hopping Parameter*, Phys. Rev. B **99,** 205134 (2019).

[45] J. Liu, J. Liu, and X. Dai, *The Pseudo-Landau-Level Representation of Twisted Bilayer Graphene: Band Topology and the Implications on the Correlated Insulating Phase*, Phys. Rev. B **99,** 155415 (2019).

[46] H. C. Po, H. Watanabe, and A. Vishwanath, *Fragile Topology and Wannier Obstructions*, Phys. Rev. Lett. **121,** 126402 (2018).

[47] A. Jorio, L. G. Cançado, and L. M. Malard, *Vibrations in Graphene*, in *2D Materials: Properties and Devices*, edited by P. Avouris, T. F. Heinz, and T. Low (Cambridge University Press, Cambridge, England, 2017), pp. 71–89.

[48] A. I. Cocemasov, D. L. Nika, and A. A. Balandin, *Phonons in Twisted Bilayer Graphene*, Phys. Rev. B **88,** 035428 (2013).

[49] Y. Jiang, J. Mao, X. Lai, K. Watanabe, T. Taniguchi, K. Haule, and E. Y. Andrei, *Evidence of Charge-Ordering and Broken Rotational Symmetry in Magic Angle Twisted Bilayer Graphene*, Nature (London) **573,** 91 (2019).

[50] S. Liu, E. Khalaf, J. Y. Lee, and A. Vishwanath, *Nematic Topological Semimetal and Insulator in Magic Angle Bilayer Graphene at Charge Neutrality*, arXiv:1905.07409.

[51] M. Fabrizio, M. Airoldi, and E. Tosatti, *Interplay of Orbital Degeneracy and Superconductivity in a Molecular Conductor*, Phys. Rev. B **53,** 12086 (1996).

[52] M. Fabrizio and E. Tosatti, *Nonmagnetic Molecular Jahn-Teller Mott Insulators*, Phys. Rev. B **55**, 13465 (1997).

[53] M. Capone, M. Fabrizio, C. Castellani, and E. Tosatti, *Strongly Correlated Superconductivity and Pseudogap Phase Near a Multiband Mott Insulator*, Phys. Rev. Lett. **93**, 047001 (2004).

[54] C. Xu and L. Balents, *Topological Superconductivity in Twisted Multilayer Graphene*, Phys. Rev. Lett. **121**, 087001 (2018).

[55] G. Baskaran, *Theory of Emergent Josephson Lattice in Neutral Twisted Bilayer Graphene (Moiré is Different)*, arXiv:1804.00627.

[56] J. F. Dodaro, S. A. Kivelson, Y. Schattner, X. Q. Sun, and C. Wang, *Phases of a Phenomenological Model of Twisted Bilayer Graphene*, Phys. Rev. B **98**, 075154 (2018).

[57] H. Isobe, N. F. Q. Yuan, and L. Fu, *Unconventional Superconductivity and Density Waves in Twisted Bilayer Graphene*, Phys. Rev. X **8**, 041041 (2018).

[58] D. M. Kennes, J. Lischner, and C. Karrasch, *Strong Correlations and $d + id$ Superconductivity in Twisted Bilayer Graphene*, Phys. Rev. B **98**, 241407 (2018).

[59] C.-C. Liu, L.-D. Zhang, W.-Q. Chen, and F. Yang, *Chiral Spin Density Wave and $d + id$ Superconductivity in the Magic-Angle-Twisted Bilayer Graphene*, Phys. Rev. Lett. **121**, 217001 (2018).

[60] Y.-H. Zhang, D. Mao, Y. Cao, P. Jarillo-Herrero, and T. Senthil, *Nearly Flat Chern Bands in Moiré Superlattices*, Phys. Rev. B **99**, 075127 (2019).

[61] M. Fidrysiak, M. Zegrodnik, and J. Spałek, *Unconventional Topological Superconductivity and Phase Diagram for an Effective Two-Orbital Model as Applied to Twisted Bilayer Graphene*, Phys. Rev. B **98**, 085436 (2018).

[62] E. Laksono, J. N. Leaw, A. Reaves, M. Singh, X. Wang, S. Adam, and X. Gu, *Singlet Superconductivity Enhanced by Charge Order in Nested Twisted Bilayer Graphene Fermi Surfaces*, Solid State Commun. **282**, 38 (2018).

[63] Y. Su and S.-Z. Lin, *Pairing Symmetry and Spontaneous Vortex-Antivortex Lattice in Superconducting Twisted-Bilayer Graphene: Bogoliubov–de Gennes Approach*, Phys. Rev. B **98**, 195101 (2018).

[64] X. Gu, C. Chen, J. N. Leaw, E. Laksono, V. M. Pereira, G. Vignale, and S. Adam, *Antiferromagnetism and Chiral d-Wave Superconductivity from an Effective $t - J - D$ Model for Twisted Bilayer Graphene*, arXiv:1902.00029.

[65] J. González and T. Stauber, *Kohn-Luttinger Superconductivity in Twisted Bilayer Graphene*, Phys. Rev. Lett. **122**, 026801 (2019).

[66] J. González and T. Stauber, *Marginal Fermi Liquid in Twisted Bilayer Graphene*, arXiv:1903.01376.

[67] B. Roy and V. Juričić, *Unconventional Superconductivity in Nearly Flat Bands in Twisted Bilayer Graphene*, Phys. Rev. B **99**, 121407 (2019).

[68] L. Classen, C. Honerkamp, and M. M. Scherer, *Competing Phases of Interacting Electrons on Triangular Lattices in Moiré Heterostructures*, Phys. Rev. B **99**, 195120 (2019).

[69] H. Guo, X. Zhu, S. Feng, and R. T. Scalettar, *Pairing Symmetry of Interacting Fermions on a Twisted Bilayer Graphene Superlattice*, Phys. Rev. B **97**, 235453 (2018).

[70] T. Huang, L. Zhang, and T. Ma, *Antiferromagnetically Ordered Mott Insulator and $d + id$ Superconductivity in Twisted Bilayer Graphene: A Quantum Monte Carlo Study*, Sci. Bull. **64**, 310 (2019).

[71] Yu-P. Lin and R. M. Nandkishore, *A Chiral Twist on the High-T_c Phase Diagram in Moiré Heterostructures*, Phys. Rev. B **100**, 085136 (2019).

[72] F. Wu, A. H. MacDonald, and I. Martin, *Theory of Phonon-Mediated Superconductivity in Twisted Bilayer Graphene*, Phys. Rev. Lett. **121**, 257001 (2018).

[73] B. Lian, Z. Wang, and B. A. Bernevig, *Twisted Bilayer Graphene: A Phonon Driven Superconductor*, Phys. Rev. Lett. **122**, 257002 (2019).

[74] M. Sigrist and K. Ueda, *Phenomenological Theory of Unconventional Superconductivity*, Rev. Mod. Phys. **63**, 239 (1991).

[75] V. Kozii, H. Isobe, J. W. F. Venderbos, and L. Fu, *Nematic Superconductivity Stabilized by Density Wave Fluctuations: Application to Twisted Bilayer Graphene*, Phys. Rev. B **99**, 144507 (2019).

[76] L. Lindsay and D. A. Broido, *Optimized Tersoff and Brenner Empirical Potential Parameters for Lattice Dynamics and Phonon Thermal Transport in Carbon Nanotubes and Graphene*, Phys. Rev. B **81**, 205441 (2010).

[77] A. N. Kolmogorov and V. H. Crespi, *Registry-Dependent Interlayer Potential for Graphitic Systems*, Phys. Rev. B **71**, 235415 (2005).

[78] W. Ouyang, D. Mandelli, M. Urbakh, and O. Hod, *Nanoserpents: Graphene Nanoribbon Motion on Two-Dimensional Hexagonal Materials*, Nano Lett. **18**, 6009 (2018).

[79] E. Bitzek, P. Koskinen, F. Gähler, M. Moseler, and P. Gumbsch, *Structural Relaxation Made Simple*, Phys. Rev. Lett. **97**, 170201 (2006).

[80] E. Koukaras, G. Kalosakas, C. Galiotis, and K. Papagelis, *Phonon Properties of Graphene Derived from Molecular Dynamics Simulations*, Sci. Rep. **5**, 12923 (2015).

[81] D. L. Nika and A. A. Balandin, *Two-Dimensional Phonon Transport in Graphene*, J. Phys. Condens. Matter **24**, 233203 (2012).

[82] D. M. Basko and I. L. Aleiner, *Interplay of Coulomb and Electron-Phonon Interactions in Graphene*, Phys. Rev. B **77**, 041409 (2008).